Physics of the Earth and Planetary Interiors 343 (2023) 107087

Contents lists available at ScienceDirect

Physics of the Earth and Planetary Interiors

journal homepage: www.elsevier.com/locate/pepi

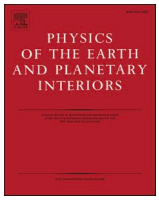

Investigation of the porosity of L/LL4 ordinary chondrite Bjurböle using synchrotron radiation microtomography and scanning electron microscopy: Implications for parent body evolution

A.-J. Soini [a,*], I.T. Kukkonen [a], H. Suhonen [b], B. Lukić [c], T. Kohout [a,d], A.V. Luttinen [e]

[a] Department of Geosciences and Geography, University of Helsinki, P.O. Box 68, FI-00014 Helsinki, Finland
[b] Department of Physics, University of Helsinki, P.O. Box 64, FI-00014 Helsinki, Finland
[c] ESRF – The European Synchrotron, CS 40220, F-38043 Grenoble, Cedex 9, France
[d] Institute of Geology of the Czech Academy of Sciences, Rozvojova 269, 16500 Prague 6, Czech Republic
[e] Finnish Museum of Natural History, University of Helsinki, P.O. Box 44, FI-00014 Helsinki, Finland

ARTICLE INFO

Keywords:
Bjurböle
Ordinary chondrites
Porosity
Thermal evolution
Synchrotron radiation microtomography
Scanning electron microscopy

ABSTRACT

Porosity is an essential property of chondritic meteorites and is closely related to the genesis, thermal evolution, metamorphism, and thermal properties of the meteorite parent bodies. We study porosity, its texture, and shapes at sub-micron resolution in 3D and 2D within a 0.35 cm^3 sample of the L/LL4 ordinary chondrite (OC) Bjurböle using two techniques, synchrotron radiation microtomography (SRμCT) and scanning electron microscopy (SEM). We employ automated segmentation tools that can be applied to both SRμCT and SEM data. Successful segmentation results can be achieved by combining visual qualitative examination and machine learning algorithms.

We report novel measurement results of three-dimensional porosity properties of Bjurböle, such as aspect ratio and connectivity of void spaces, and compare the results of 2D and 3D porosity analysis. The Bjurböle sample in this study is a complex, highly porous, and friable medium and the dominant type of porosity is intergranular, continuous porosity, which contains almost all porosity volume. The shapes of the void volumes have an important effect on the connectivity of the porosity and thermal transport properties. Positive correlations between void diameter and aspect ratio as well as void volume and connectivity are present in Bjurböle, which indicate that smaller voids have lower aspect ratios and lower connectivity. In Bjurböle, small, near-spherical voids with few connections have the highest relative frequency, whereas larger void spaces with higher aspect ratios and connectivity are significantly fewer. Completely isolated pores, i.e., voids surrounded by solid material, also have a high relative frequency, and they exist within the chondrules and the matrix. However, the volume percentage of these pores is negligible compared to that of the continuous porosity.

Our results support the previously measured high porosities of Bjurböle. The volume percentage of intergranular void spaces, in particular in the matrix, and the measured high porosities are not in line with the results of thermal evolution and sintering models of chondritic parent bodies regarding petrologic type 4, which implies that Bjurböle originates from a parent body with an initial onion shell structure that fragmented during or after its metamorphic peak and quickly reaccreted into a rubble pile.

1. Introduction

Meteorites have remarkable scientific value as they represent diverse types of solar system bodies and store a record of the early solar system and its chemical and physical conditions (Jones, 2003; Flynn et al., 2018). Porosities of chondrite samples have direct implications for the evolution of the parent bodies, their thermal properties, and thermal evolution as well as for understanding the properties of asteroids, comets, and planetary satellites at present (e.g., Opeil et al., 2020; Ostrowski and Bryson, 2019; Opeil et al., 2012). Ordinary chondrite (OC) falls demonstrate high porosities averaging from 7 to 14 vol% (Flynn et al., 2018; Soini et al., 2020). OC finds have lower porosities on

* Corresponding author.
E-mail address: assi-johanna.soini@helsinki.fi (A.-J. Soini).

https://doi.org/10.1016/j.pepi.2023.107087
Received 30 April 2022; Received in revised form 10 July 2023; Accepted 8 August 2023
Available online 9 August 2023

average ranging from 2.8 to 5.8 vol% (Macke, 2010), which may be due to weathering products that occupy the pore space.

We study the porosity properties of ordinary chondrite Bjurböle at sub-micron resolution. Bjurböle is a fall classified as L/LL4 OC of shock stage S1 and weathering index W0 (Grady, 2000; Maksimova et al., 2021). Bjurböle is exceptional in its class. It is highly friable and not well consolidated with poorly attached chondrules (Ramsay and Borgström, 1902) albeit being thermally metamorphosed and subjected to recrystallization at approximately 600–700 °C (Macke, 2010). Most of the recovered Bjurböle fragments have high porosities close to 20% (e.g., Kohout et al., 2017; Macke, 2010) but also samples that do not demonstrate as high porosities or friability have been reported (Andre et al., 2003). The physical properties and size range from grams to tens of kilograms of the recovered Bjurböle meteorites indicate that the Bjurböle meteoroid may have had a heterogeneous distribution of strength and porosity and it may consist of both weak zones and coherent areas (Kohout et al., 2017). Thermal evolution models (e.g., Henke et al., 2012; Harrison and Grimm, 2010; Hellmann et al., 2019; Edwards and Blackburn, 2020) suggest that OCs come from parent bodies of about 100–150 km in diameter. Paleomagnetic data of a Bjurböle meteorite (Bryson et al., 2019) imply the Bjurböle parent body had a radius of 150–200 km.

Bulk porosity of a meteorite can be determined with a gas pycnometer or according to the Archimedes principle (e.g., Flynn et al., 1999; Consolmagno and Britt, 1998; Soini et al., 2020). Pore locations and structures can be mapped using scanning electron microscopy (SEM) (e.g., Strait, 2010) and X-ray microtomography (e.g., Friedrich et al., 2008; Lewis et al., 2018). X-ray microtomography is the only nondestructive technique that provides three-dimensional information about the porosity structure. Although the resolution of SEM exceeds that of X-ray microtomography, even a nanometer resolution can be achieved using high-resolution synchrotron radiation microtomography (SRμCT).

SRμCT and lower resolution laboratory systems of X-ray microtomography have been used in meteoritics (e.g., Farbaniec et al., 2021; Rutherford et al., 2017; Friedrich and Rivers, 2013; Hezel et al., 2013) but mostly to study grain and chondrule size distributions (e.g., Friedrich et al., 2021). Previous X-ray microtomography investigations of planetary materials have been reviewed in Ebel and Rivers (2007) and Hanna and Ketcham (2017).

The chondrules, mineralogy, and isotope composition of Bjurböle have been studied extensively (e.g., Friedrich et al., 2008b; Rushmer et al., 2013; Florin et al., 2020; Maksimova et al., 2021). The few studies of its porosity have mostly utilized the Archimedes principle (Terho et al., 1993) and gas pycnometry (Wilkison et al., 2003; Kohout et al., 2017).

The aim of this study is to quantify porosity properties, such as aspect ratios of void spaces, of Bjurböle in 2D and 3D using SEM in backscattered electron mode (BSE) and SRμCT at sub-micron resolution. To our knowledge, three-dimensional porosity properties of Bjurböle have not been reported in previous studies. We examine techniques for image post-processing that can be applied to both imaging techniques. We compare the 2D porosity results of the BSE mosaic of a polished section with the results obtained from the high-resolution SRμCT scanned volumes, at comparable resolution. In addition, we compare 2D porosity results of selected areas on the section surface obtained from the BSE image and the corresponding 2D SRμCT slice, at comparable resolution. Furthermore, we report the results of 3D porosity analysis obtained from the low-resolution SRμCT scanned bulk sample.

We discuss the accretion and thermal evolution of Bjurböle using the porosity values and textures obtained in this study, theoretical models of thermal evolution of OC parent bodies (e.g., Yomogida and Matsui, 1984; Henke et al., 2012; Lucas et al., 2020), and experimental results of friable and porous ordinary chondrites (Wilkison et al., 2003; Sasso et al., 2009; Kohout et al., 2017). We show that our porosity results support the rubble pile evolution model for Bjurböle.

2. Materials and methodology

Throughout this work, we refer to porosity as the total of all void spaces present within the sample, whereas pore space is the continuous and interconnected void space, and a pore is a void surrounded by the solid meteoritic material (Allaby, 2020). Thus, void spaces refer to all porosity types, such as pores, cracks, and gaps.

2.1. Sample and bulk properties

The 1.0 cm × 0.8 cm × 0.8 cm sample of Bjurböle was obtained from the meteorite collection of the Finnish Museum of Natural History, University of Helsinki. We measured the mass of the Bjurböle sample using an Ohaus Scout Pro scale with a resolution of 0.01 g. The grain volume, i.e., the volume of the mineral grains, was measured using a Quantachrome Ultrapyc 1200e gas pycnometer. The bulk volume that contains the volume of the mineral grains and the volume of the void spaces was determined by a NextEngine 3D Scanner Ultra HD model 2020i laser scanner. The grain and bulk densities were calculated from the measured grain and bulk volumes and the sample mass. The porosity of the whole sample was then calculated from the obtained grain and bulk density. The measured values for mass, grain volume, and bulk volume are 0.95 g, 0.26 cm^3, and 0.35cm^3, respectively, and the calculated values for grain density and bulk density are 3.63 g/cm^3 and 2.84 g/cm^3, respectively. The calculated bulk porosity of the sample is 21.9 ± 0.6 vol%. All the above measurements as well as SRμCT were performed on the sample without any sample preparation.

To study the sample using SEM, we prepared a polished section on which we also conducted elemental analyses using an energy dispersive spectrometer (EDS) attached to SEM. The entire section was imaged using SEM (Soini et al., 2022) (Fig. 1) and three subregions were cropped from the section to match the high-resolution SRμCT regions (Soini et al., 2023) to compare porosity results. In Fig. 1, high-density regions are shown as bright and low-density regions, such as air in the void space, as darker (Dubetz, 2016). The justification for selecting the areas/volumes is that they appear to have different chondrule-matrix ratios and thus represent the heterogeneity within the bulk sample. These areas and their respective high-resolution SRμCT volumes are hereafter referred to as Area 1 and Volume 1, Area 2 and Volume 2, and Area 3 and Volume 3 (Fig. 1). The Areas 1–3 are ~1.9 mm^2, the polished section is ~23.5 mm^2, and the Volumes 1–3 are ~2.6 mm^3.

The sample shows typical petrographic characteristics of Bjurböle chondrite. Olivine porphyritic, olivine-pyroxene porphyritic, pyroxene porphyritic, barred olivine, and radial pyroxene type chondrules and chondrule fragments are set in a matrix of olivine, pyroxene, troilite, Fe—Ni metal, minor chromite and apatite, and trace amounts of a Ti-rich phase. Based on visual inspection, chondrules occupy approximately 45% of the section. The matrix is fine-grained with a typical grain size of ~0.01–0.02 mm. The intact chondrules range from ~0.1 to ~1.5 mm in diameter with an average of ~0.45 mm. Relatively Al-, Na-, and Ca-rich parts (likely feldspar) indicate recrystallized glassy mesostasis in the chondrules. Area 1 is occupied predominantly by an elongated large (~1.5 mm) olivine-pyroxene porphyritic type chondrule (Chondrule 1) dominated by low-Ca pyroxene. The chondrule also contains large grains of troilite and Fe—Ni metal and a large void ~60 μm in diameter in the middle (Fig. 1). Area 2 is dominated by an elongated large (~1 mm) radial pyroxene type chondrule (Chondrule 2) composed mainly of sub-parallel plates of low-Ca pyroxene. The chondrule is partially rimmed by troilite. Area 3 contains several relatively small chondrules. The largest of them is ~0.8 mm in diameter. It is a round, very fine-grained radial pyroxene type chondrule characterized by rims enriched with fine-grained troilite, whereas the others are olivine porphyritic type chondrules, many of which are partially broken. Visual inspection reveals small cracks within the chondrules and the matrix. Intragrain cracks have varying widths generally <5 μm. The widths of the gaps surrounding the chondrules typically vary between 10 μm and 20 μm. In

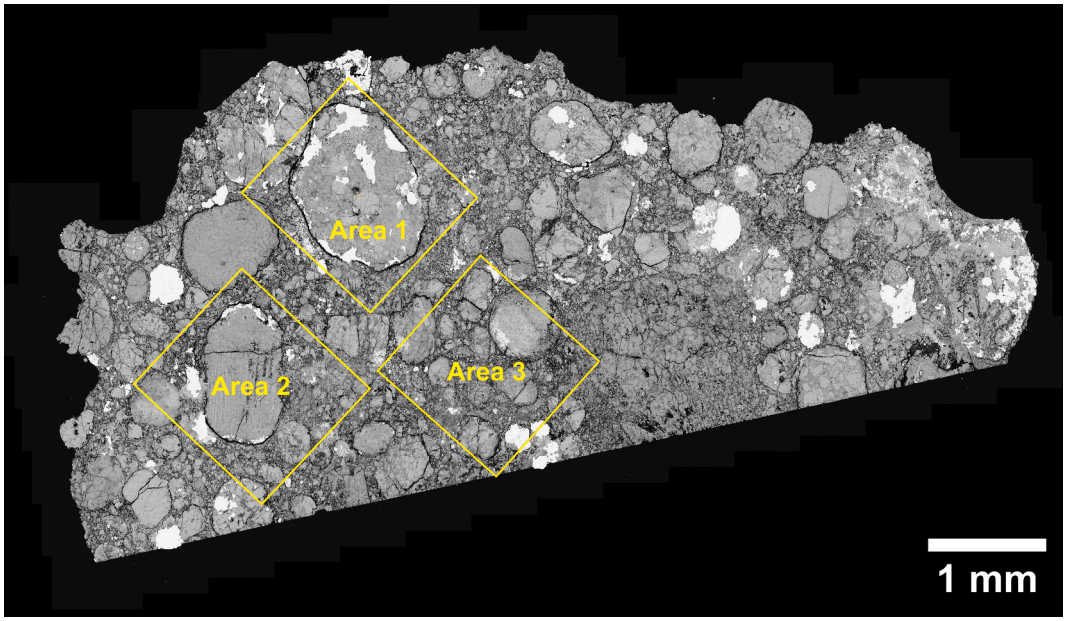

Fig. 1. The polished section used in porosity analyses constructed of stitched BSE images. The boxes indicate the locations of the analyzed areas used in SEM analysis and corresponding volumes used in SRμCT analysis.

places, the gap may even have a width of approximately 40 μm. The widths of the intergrain cracks are of the order of a few microns.

2.2. Image acquisition

2.2.1. SRμCT

SRμCT was performed at the European Synchrotron Radiation Facility (ESRF) using a microtomography setup installed on a 145 m long imaging beamline ID19. Two imaging configurations were used, one for low-resolution (LR) and another for high-resolution imaging (HR). A filtered pink beam, generated by a wiggler insertion device, was used to produce a polychromatic energy spectrum that illuminates the sample with a peak energy of ~65 keV (LR) or ~ 78 keV (HR) to have sufficient transmission through the sample. The beam is shaped by the first series of slits (~30 m from the source) and filtered with mandatory permanent optical elements (1 mm diamond window and series of thin carbon windows) together with 2.8 mm aluminum within the first series of attenuators to reduce the heat load contribution of the low energy spectrum emitted by the insertion device. In addition, 0.7 mm copper and 0.07 mm tungsten attenuators are used within the second series of attenuators to tune the spectrum to the above-mentioned peak energy with final beam size shaping by secondary slits (~135 m from the source). In the case of HR, additional focusing elements (38 CRL-compact refractive lenses) were used to focus the beam required by a relatively small field of view. The resulting photon density from the focusing elements required only marginal tuning of the insertion device gap, which allowed conducting the tomography scans at relatively similar peak energy and with a comparable spectrum at both imaging resolutions, i.e., the densities at LR and HR appear relatively similar. The X-ray detector was placed downstream from the sample (2.82 m for LR, 0.1 m for HR) in order to form propagation-based phase contrast. This contrast mode enhances the edges (such as between the pore and the matrix) and gives access to quantitative density measurement. Indirect detector systems were used in both imaging cases consisting of a scintillator and a relay mirror optically coupled to pco.edge 5.5 camera. Single crystal LuAG:Ce scintillator was used to convert the transmitted spectrum into a luminescence image, which is relayed to the camera via a mirror, allowing the detector to be perpendicular to the X-ray propagation axis. The thickness of the used scintillator directly influences the spatial resolution of the imaging assembly and was, in the present case, 500 μm for LR and 25 μm for HR. The optics used had either 1× magnification (100:100 Hasselblad lens assembly) leading to 6.5 μm pixel size (LR) or 10× magnification (Mitutoyo M Plan APO NA = 0.28) leading to 0.65 μm pixel size (HR). Thus, the voxel edge lengths of LR and HR are 6.5 μm and 0.65 μm, respectively. For the tomography scans, the sample was rotated continuously over 360 degrees, and either 4000 projections with 50 ms exposure time (LR) or 10,000 projections with 100 ms exposure time were taken (HR). A phase retrieval algorithm (Paganin et al., 2002) was used to treat the projections before tomographic reconstruction with filtered backprojection using the Nabu software (GitLab, 2022). The size of the cylindrical field of view in the 3D images was 16 mm × 10 mm (diameter x height) for the LR scans and 1.6 mm × 1.4 mm for the HR scans. The LR scans produced a 3D image that contains the whole sample, while the HR scans produced 3D images corresponding to Areas 1–3 (Soini et al., 2023). Fig. 2 shows a 3D rendering of the low-resolution SRμCT data of the whole sample (Plot A) and the chosen SRμCT slice that encloses Areas 1–3 (Plot B) visualized using Drishti software (Limaye, 2012).

2.2.2. SEM

After SRμCT, the sample was cut along such a plane that the SRμCT 3D density models could be analyzed with SEM. The sample was mounted in epoxy to cut the section that contains all the regions imaged using HR SRμCT. We compared the virtual slices of the LR SRμCT data to the sample block-face and its outlines to identify the correct imaging plane. The section surface was polished until its outlines matched those of the SRμCT slice. Although the angle of the SRμCT slice relative to the sample was determined from the 3D model, the section surface was cut and polished manually, thus resulting in a slightly different angle and a slightly different field of view, i.e., different depth of the imaging frame, compared to the SRμCT slice. Computerized and automated cutting of the section using the precise angle would improve the results and lead to the same field of view than that of the SRμCT slice. The polished surface was then coated with a thin layer of carbon using Cressington 208carbon High Vacuum Carbon Coater.

SEM was performed using The JEOL JSM-5900 LV SEM in back-scattered electron mode (BSE) with an accelerating voltage for the electrons of 15 kV and stage height of 10 mm. We collected 121 overlapping images (Soini et al., 2022) to get a field of view of the whole sample surface. The images were stitched together using the pairwise

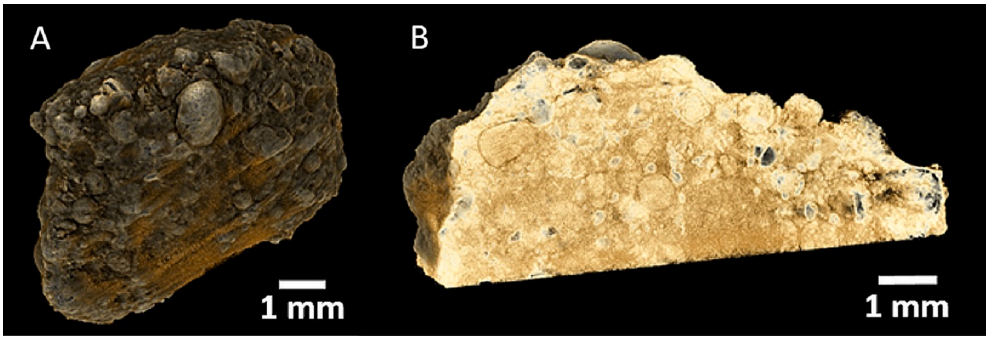

Fig. 2. 3D rendering of the low-resolution SRμCT image stack of the entire Bjurböle sample (A) and the chosen slice for porosity analyses (B) visualized using Drishti software.

stitching plugin (Preibisch et al., 2009) in the image processing toolkit *Fiji* (Schindelin et al., 2012) to create a mosaic of the surface with a pixel size of 0.55 μm (Fig. 1). The BSE mosaic displays similar outlines as the chosen SRμCT slice in Fig. 2.

The HR SRμCT slice corresponding to the BSE image was determined by visual inspection of the structures on the section surface and their locations in the SRμCT stack. When the search was narrowed down to only tens of slices and thus approximately 6.5 μm thick volume, we resolved the slice closest to the section surface by comparing their porosities. We estimate that an error of ±0.05 area% in porosity determination may be introduced by not 100% matching the SRμCT image to the BSE image based on the average difference in porosity at 0.65 μm slice spacing in the 6.5 μm thick sub-volume within the SRμCT stack.

2.3. Image segmentation

Segmenting air-filled void spaces from the solid meteorite results in a binary map of the porosity structure in which voids and solid are represented by only two intensity values. However, meteorites are intricate porous media and shallow, filled or partially filled void spaces, and unclear void boundaries possibly due to the microporosity below the imaging resolution (Dubetz, 2016) complicate the segmentation, which is the most crucial step in image processing directly affecting the precision of the following analysis results (Song et al., 2019). Thus, we applied filters to denoise the SRμCT images, to enhance their contrast, and to accentuate their details. Ring artifacts in the SRμCT data possibly produced by the reconstruction or the irregular response of the detecting system were handled by combined wavelet–fast Fourier transform filtering (Münch et al., 2009). We used *Transform 2D 3D* and *Stripes Filter* tools in *Xlib* plugin (Münch et al., 2009) in *Fiji* to first convert the SRμCT stacks from cartesian coordinates to spherical coordinates and then to filter the vertical stripes. We used Daubechies wavelets of different size depending on the image stack and chose the values for the highest decomposition level and damping coefficients based on the spatial frequency spectrum of the stripes, which correlates with the width of the stripes (Münch et al., 2009). To avoid loss of valid information, these values were selected as small as possible (Münch et al., 2009).

Hundreds of semiautomatic and automatic algorithms have been developed to find suitable thresholds (Arganda-Carreras et al., 2017) to binarize an image. Visual qualitative examination and quantitative comparison of image porosity govern the criteria for assessing a suitable algorithm (Song et al., 2019). In our study, the grayscale histogram was not a suitable means to accurately segment the SRμCT images because of the ring artifacts and the overlap of the attenuation peaks in the histograms generated during the imaging process. Additionally, SRμCT may result in partial volume averaging where a voxel characterizes more than one component (Ginat and Gupta, 2015). Thus, some of the histograms were not bimodal as expected for the grayscale distribution but multimodal or demonstrated a single peak with a widened base due to the noise (see also Dubetz, 2016). Even though the noise was reduced by filtering, the segmentation results were not satisfactory and user-dependent manual segmentation was required as well. *Trainable Weka Segmentation (TWS)* (Arganda-Carreras et al., 2017) and *Labkit* (Arzt et al., 2022) plugins in *Fiji* allow including this additional knowledge in the segmentation. We applied *TWS* to train a classifier to segment 2D BSE images and SRμCT slices. Using the same classifier for datasets obtained using different methods means that the segmentation is based on the same ground truth and the porosity results can be compared with each other. *Labkit* is especially designed for big image data, and therefore we used it to train classifiers to segment the HR and LR 3D data. A description of the use of the plugins is given below in section 2.3.1.

We used a threshold value of 100 to segment the BSE mosaic of the entire polished section. We estimate that our porosity determination using thresholding likely results in an error of ±1.0 area% since lowering/rising the threshold value by one results in approximately ±0.3 area% change in porosity determination.

Based on visual examination of the segmentation results, we applied morphological operators (opening and closing) for binarized images when appropriate to retrieve the segmented geometry as closely as possible. We estimate that these operations result in errors of ±0.5 area % and ± 1 vol% in porosity determination based on comparing the determined porosity values before and after applying the operators.

2.3.1. Trainable WEKA Segmentation and Labkit

TWS integrates *Fiji* and machine learning algorithms of the *Waikato Environment for Knowledge Analysis (WEKA)* toolkit (Hall et al., 2009). The efficiency of *Labkit* is based on processing image chunks in parallel using *ImgLib2* (Pietzsch et al., 2012) to support chunked memory handling and *BigDataViewer* as well as the option of implementing OpenCL kernels that enable fast graphics processing units (GPU) computations (Haase et al., 2020) to build up additional runtime performance (Arzt et al., 2022).

The foundation of both plugins is the random forest-based pixel classification algorithm. The pipeline for pixel classification consists of extracting the image features from the input image, defining a set of pixel samples representing ground truth classes, and deriving feature vectors of float values from the sample pixels (Arganda-Carreras et al., 2017; Arzt et al., 2022). Each pixel in the image represents both intensity and the image features within its area (William et al., 2019). The feature vectors of all labeled pixels are combined with their respective classes, which establishes the training set used to create the random forest classifier which can be applied to automatically classify the rest of the input pixels or completely new data (Arganda-Carreras et al., 2017; Arzt et al., 2022).

We trained the pixel level classifier on porosity, solid phase, and background where applicable. We added markers to the classes using the tools for line and region of interest (ROI) drawing in *Fiji*, i.e., selected pixels that were assigned to a relevant class. Processing images using filters before segmentation may increase noise, and therefore we applied several different noise reduction filters available in *TWS* and *Labkit*. In

TWS, we selected 172 image features computed by spherical filters with radii varying from 1 to 16 pixels to train the classifier including 1) Noise reduction filters: *Gaussian blur*, *Kuwahara* (Bartyzel, 2016), and *Bilateral filters* that have been reported to remove noise efficiently whilst preserving the edges (Francis and De Jager, 2005), 2) Edge detectors: *Hessian matrix eigenvalues* (Tankyevych et al., 2008), *Sobel filter* (Biswas and Ghoshal, 2016), *Gabor filter* (Chang and Morgan, 2014), and *Difference of Gaussians* that indicate boundaries of objects in the image (Arganda-Carreras et al., 2017), 3) Texture filters: *mean*, *median*, *minimum*, *maximum*, *variance*, and *entropy filters* that extract texture information, and 4): *Membrane projections* that detect and localize objects. In *Labkit*, we also applied *Gaussian gradient magnitude* and *Laplacian of Gaussian* edge detectors. Each filter generates an output image, and one image is created for each feature (Arzt et al., 2022). We used the default classifier option in *TWS*, i.e., FastRandomForest. It is a reimplementation of the Random Forest classifier for Java by Fran Supek initialized with 200 trees each constructed while considering two random features. *Labkit* uses the FastRF library (Supek, 2015) that consists of 100 decision trees. We corrected and added labels to the classifier output on-the-fly to optimize the training and to improve the probability of successful segmentation. Additionally, *Labkit* allows label curation and curation of segmentation results to resolve the remaining errors made by the classifier to achieve a satisfactory segmentation result for analysis (Arzt et al., 2022).

The out-of-bag error, which describes the prediction error of the random forest, for the *TWS* classifier was maintained under 5%. The results of the accuracy tests of fast-random-forest of Supek (2015) exceed 90% on average. *Labkit* obtained scores of 0.793 for segmentation accuracy and 0.997 for detection accuracy in Cell Tracking Challenge (CTC, 2021) (Arzt et al., 2022).

To get an estimate of the segmentation accuracy, we compared manual and automatic segmentation on a subset of an image stack. At times, automatic segmentation resulted in errors that do not correspond to the original image. However, these errors can be corrected during the training or by manual curation of the segmentation result, which improves the average precision. Based on the comparison of the segmentation results and the prediction errors, we estimate that an error of ±1.5–4 vol% in porosity determination may be introduced by the pixel classification method.

2.4. Image analysis

2.4.1. Representative elementary area and volume

Representative elementary area (REA) and representative elementary volume (REV) are defined as the minimal area and volume large enough to be statistically representative of the sample and contain all possible porosity types in the macroscopic sample (Song et al., 2019; Drugan and Willis, 1996; Galli et al., 2012). Since the field of view of BSE and SRμCT images may be small, it is important to determine whether the porosity results derived from these images are plausible and characterize the porosity and its structure of the entire sample (Song et al., 2019).

We used box-counting and representative elementary volume (REV) functions of *Porespy*, which is a *Python* toolkit for quantitative analysis of porous media images (Gostick et al., 2019), to find out if REA or REV exist. Both the box-counting and REV functions can be applied to 2D and 3D data, and they are based on binary images of voids and solid. Box counting function calculates the fractal dimension, i.e., the ratio of the change in detail to the change in scale, and REA or REV is resolved based on its variation (Zhang et al., 2018). Areas/volumes of large porosity have a higher ratio of matrix to chondrules as well as complex and irregular structures and thus high fractal dimension defined by both the porosity and its structure (Zou et al., 2020). REV function calculates the porosity of the image as a function of subdomain size (Gostick et al., 2019). REA and REV are determined as a subdomain size or volume beyond which the porosity remains stable with negligible variation (Zhang et al., 2018). Both approaches gave a comparable REA of approximately 1.4 mm^2. The calculated REV is approximately 1.9 mm^3.

2.4.2. Quantification of porosity properties

Void diameter can be determined as Feret diameter, which measures the longest line segment that fits the void space, or as equivalent diameter, which demonstrates the largest inscribed sphere that fits within the void space (Dubetz, 2016). Although Feret diameter is computationally more expensive compared to the equivalent diameter, it is more accurate and capable of handling irregular shapes (Dubetz, 2016) and thus the chosen method in this study.

We used *Dragonfly* software version 2022.2 (Object Research Systems (ORS) Inc., Montreal, Canada, 2020) to quantify the porosity properties. Before quantification, the region of interest was refined by removing pixels/voxels by count three to avoid quantization of the results and to accurately analyze a discrete void space (Hanna and Ketcham, 2017; Ketcham and Hildebrandt, 2014). We applied connected components analysis to group the void spaces into labeled components based on connectivity. We applied 6-connected connectivity, which leads to the maximum number of labeled components. It determines how a voxel relates to its neighbors by using the six faces adjacent to the voxel. We computed the minimum, mean, and maximum Feret diameters as well as the areas/volumes for each connected component, i.e., void space. Aspect ratio is the ratio of void size to void throat size and can be calculated as the ratio of maximum to minimum Feret diameter. *Dragonfly* calculates the maximum and minimum Feret diameters as the longest or shortest distance between any two parallel tangents along each component's convex hull, respectively. Mean Feret diameter is calculated as the mean value of the minimum and maximum Feret diameters of each component's boundary over a sufficient number of orientations.

Pore network modeling in *Dragonfly* allows the investigation of the inter-relationship between connected components by employing the University of Waterloo's *OpenPNM* package (Gostick et al., 2016). *OpenPNM* treats a porous medium as a volume-averaged continuum and creates a model of the void space with spheres and lines representing the voids and their connections (Gostick et al., 2016). We modeled the void space of the entire sample (LR SRμCT) and Volumes 1–3 (HR SRμCT) and computed the number of connections the voids have with other void spaces from the created connectivity graphs.

3. Results

The results of the porosity analysis include all void spaces, i.e., detected absolute porosity, and thus all porosity types, such as pores, cracks, and gaps.

3.1. 2D porosity results

The segmentation result of the BSE mosaic of the entire section using a threshold value of 100 is shown in Fig. 3. The segmented void spaces are shown in black colour and the pixel size of the mosaic is 0.55 μm.

HR SRμCT slices of Areas 1, 2, and 3 and corresponding BSE images along with respective binary images used in the porosity analyses are presented in Supplementary material (Supplementary Fig. 1).

To compare the SRμCT results with the SEM results, we computed the following parameters: porosity, void area/volume, void diameter represented by maximum Feret diameter, and aspect ratio of voids. Table 1 shows the results of the 2D porosity analyses of the entire polished section and Areas 1–3.

Area 1 is mostly occupied by a large chondrule separated from the matrix by a gap, and therefore its total porosity differs from those of Area 2 and Area 3, which contain a higher abundance of fine-grained, porous chondrite matrix.

Fig. 4 shows the area (A) and maximum Feret diameter distribution (B) of the entire polished section. Note the logarithmic scale of relative

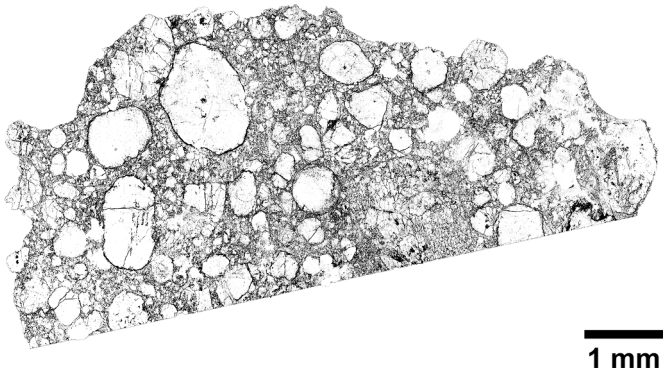

Fig. 3. The segmentation result of the entire section imaged using SEM. Void spaces segmented using a threshold value of 100 are shown in black colour.

frequency, which allows the visibility of the large values in the range that have a very low frequency. Voids with diameters ≤26 μm represent 98.4% of the void space and void areas ≤2800 μm^2 represent 99.9% of the void space in the section.

Fig. 5 shows the distribution of aspect ratios of voids (A) and the relationship between void diameter and aspect ratio of voids (B) in the polished section. The plot B in Fig. 5 is calculated from resampled data. We reduced the dataset using evenly spaced maximum Feret values and mean of the aspect ratio to visualize the ~156,000 datapoints. The computed Pearson's r in Plot B in Fig. 5 describes the value of the Pearson correlation coefficient, which is a measure of the linear trend. A weak positive correlation between void diameter and aspect ratio of voids is present in the polished section.

Aspect ratios between 2 and 3 dominate the polished section with a relative frequency of 49.8%. Voids smaller than ~250 μm show a wide range of aspect ratios, whereas most voids larger than that have quite small aspect ratios. However, a weak linear trend of increasing aspect ratio with increasing void diameter is present.

The plots of the 2D porosity results of Areas 1–3 of HR SRμCT and corresponding BSE images are provided in the Supplementary material. In all three Areas, void diameters ≤26 μm and void areas ≤2800 μm^2 represent most of the total porosity. In Area 1, the relative frequency of void diameters ≤26 μm is 87.2% in the SRμCT slice and 91.0% in the BSE image and the respective relative frequencies of void areas ≤2800 μm^2 are 99.7% and 99.7%. In Area 2, the relative frequency of void diameters ≤26 μm is 90.4% in the SRμCT slice and 92.6% in the BSE image and the respective relative frequencies of void areas ≤2800 μm^2 are 99.7% and 99.6%. In Area 3, the relative frequency of void diameters ≤26 μm is 91.5% in SRμCT slice and 92.3% in the BSE image, while the respective relative frequencies of void areas ≤2800 μm^2 are 99.6% and 99.6%. In the SRμCT slices and BSE images of Areas 1–3, the preferred aspect ratios are 2–3 (42.5%) and 1–2 (42.5%), 2–3 (43.5%) and 1–2 (48.6%), and 1–2 (70.1%) and 1–2 (66.8%), respectively. Similarly to the polished section, SRμCT slices of Areas 1–3 and BSE image of Area 3 show a weak trend of increasing aspect ratio with increasing void diameter.

Table 1
2D measurement results of pore properties of the polished section imaged using SEM and Areas 1–3 imaged using SRμCT and SEM at comparable resolution.

	Section SEM	Area 1 SRμCT	Area 1 SEM	Area 2 SRμCT	Area 2 SEM	Area 3 SRμCT	Area 3 SEM
Porosity [%]	20.8	9.5	9.9	18.1	21.5	18.4	21.9
Pixel size [μm]	0.55	0.65	0.55	0.65	0.55	0.65	0.55
Number of analyzed pores	155,919	1438	1606	1812	1691	1874	3040
Max pore area [μm^2]	754,169	31,801	41,236	173,166	178,796	36,128	27,779
Min pore area [μm^2]	0.91	1.27	0.91	1.27	0.91	2.5	1.51
Mean pore area [μm^2]	5908	322	392	1472	1550	365	274
SD of pore area [μm^2]	2423	1160	1260	4034	4438	1254	709
Max Feret diameter [μm]	4498	1077	1275	1658	1452	952	406
Min Feret diameter [μm]	0.78	0.92	0.78	0.92	0.78	0.92	0.78
Mean Feret diameter [μm]	36.4	18.6	16.6	19.5	17.5	15.6	11.3
SD of Feret diameter [μm]	18.4	49.2	42.9	46.0	43.7	34.9	22.1
Max aspect ratio	50	15	14	38	9	8.5	6.2
Min aspect ratio	1.1	1.1	1.1	1.1	1.0	1.1	1.1
Mean aspect ratio	2.5	2.6	2.3	2.5	2.1	1.9	1.8
SD of aspect ratio	1.1	1.2	1.0	1.9	0.8	0.8	0.5

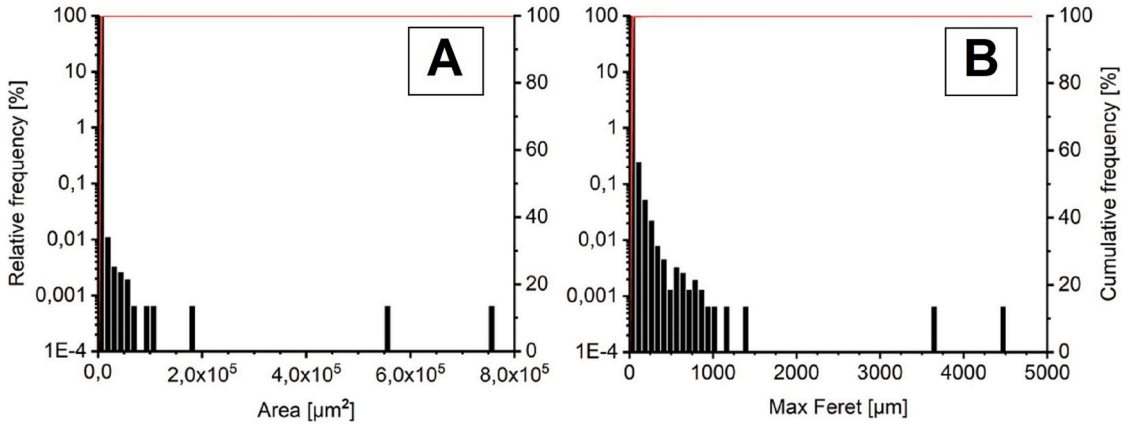

Fig. 4. Void area (A) and maximum Feret diameter (B) distributions of the BSE mosaic of the entire polished section. Maximum Feret diameter represents the void diameter and the red line represents the cumulative frequency. See section 2.4.2 for detailed definition of maximum Feret diameter. (For interpretation of the references to colour in this figure legend, the reader is referred to the web version of this article.)

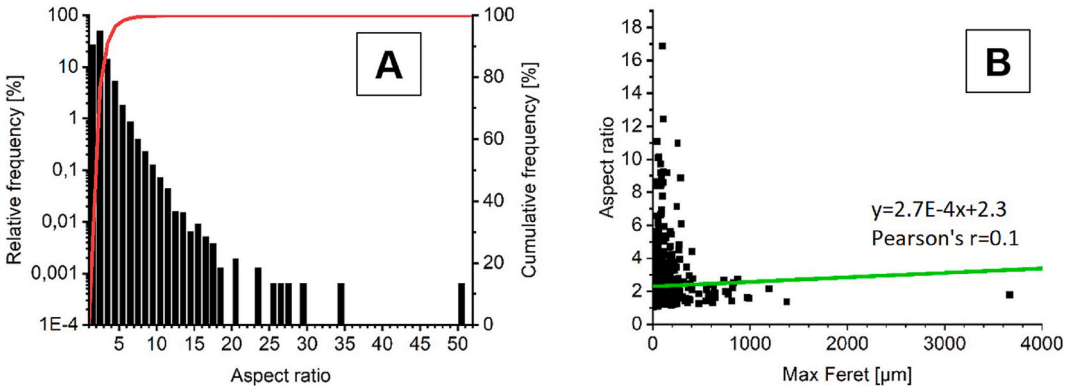

Fig. 5. Void aspect ratio distribution (A) and the relationship between maximum Feret diameter and aspect ratio of voids (B) of the BSE mosaic of the entire polished section. Maximum Feret diameter represents the void diameter. See section 2.4.2 for detailed definition of maximum Feret diameter. The red line represents the cumulative frequency, and the green line shows the linear correlation between maximum Feret diameter and aspect ratio. (For interpretation of the references to colour in this figure legend, the reader is referred to the web version of this article.)

3.2. 3D porosity results

Fig. 6 shows the 3D porosity renderings of the entire sample (LR SRμCT) and Volumes 1–3 (HR SRμCT). 3D renderings of the void space show many of the chondrules in the Bjurböle sample are surrounded by gaps and thus 3D porosity renderings also reveal the varying shapes of these chondrules. Volume 3 in Fig. 6 shows a chondrule that appears to be an elongated prolate spheroid with polar radius greater than the equatorial radius. In the BSE image of Area 3 (Fig. 1), this chondrule appears to be circular.

Measured 3D pore properties are compiled in Table 2. The plots of the 3D porosity results of the bulk sample imaged using LR SRμCT are provided in the Supplementary material.

Fig. 7 shows the void volume distributions of Volumes 1–3. Plot A in Fig. 7 displays the entire range of void volumes and plot B shows the detailed distribution of the void volumes that have high relative frequency.

In all the investigated 3D volumes, most of the total porosity volume resides in only one connected component, i.e., in the largest labeled void space, which comprises 95.2%, 96.1%, 98.4%, and 96,6% of the total porosity volume within the bulk sample, Volume 1, Volume 2, and Volume 3, respectively. The remaining porosity comprises tens of thousands of smaller void spaces that are shown in plot B in Fig. 7 and in Supplementary Fig. 6. Void volumes $\leq$5000 μm^3 represent 99.7%, 99.4%, and 99.7% of the void spaces in Volumes 1–3, respectively. In the bulk sample, void volumes $\leq$500,000 μm^3 make up 99.7% of all the voids.

Fig. 8 shows the maximum Feret diameter distribution of Volumes 1–3.

Within Volumes 1–3, 99.92%, 99.87%, and 99.95% of voids have diameters $\leq$100 μm. In the bulk sample, voids with diameters $\leq$100 μm represent 91.3% of the voids.

Fig. 9 shows the aspect ratio distribution of Volumes 1–3. The preferred aspect ratios in all the volumes are between 2 and 3 and their relative frequencies are 50.9%, 43.3%, 44.0%, and 42.2% in the bulk sample, Volume 1, Volume 2, and Volume 3, respectively.

Fig. 10 illustrates the connection between maximum Feret diameter and aspect ratio of voids in Volumes 1–3 and shows weakly or moderately positive correlations between void diameter and aspect ratio.

The plots in Fig. 10 are calculated from resampled data. The datasets contain ~120,000–145,000 data points and thus we reduced the data into smaller size with evenly-spaced maximum Feret values. The sampling interval is 0.8 μm and the sampling method is mean of the aspect ratio. Fig. 11 shows the connectivity histogram and Fig. 12 shows the relationship between void volume and connectivity of Volumes 1–3. These data are calculated from image stacks that are downsampled by a factor of two to reduce the computational cost. Thus, the spacing is increased and the number of voxels is decreased. Although, the resolution of the entire sample volume (LR SRμCT) and Volumes 1–3 (HR SRμCT) is reduced to 13 μm and 1.3 μm voxel edge length, respectively, the size of the original volume is maintained.

The relative frequencies of voids with 1–10 connections are 72.3%, 73.8%, 62.4%, and 61.8% in Volume 1, Volume 2, Volume 3, and the bulk sample, respectively. Voids with zero connections, i.e., isolated pores represent 18.3%, 13.8%, 28.0%, and 34.5% of the voids in Volume 1, Volume 2, Volume 3, and the bulk sample. There is a very high positive correlation between void volume and connectivity.

4. Discussion

4.1. Comparison of SRμCT and SEM

The most notable differences between SEM and SRμCT are that SRμCT enables three-dimensional imaging that eliminates the stereological concerns associated with SEM and direct measurement of spatial characteristics without sample preparation (Ramos Oliveira et al., 2021). 3D investigation is particularly important considering material parameters, such as (hydraulic) permeability, void tortuosity, and porosity (Kuva et al., 2018) and thus SRμCT may be the most sensible technique to study them given a sufficient resolution. SEM reveals the fine pore structures and produces data of superior resolution. However, experimental conditions govern the resolution in SRμCT and even a nanometer-scale resolution can be attained. In addition, SRμCT allows virtual sectioning and thus targeting locations of ROIs, which enhances the efficiency of other studies, e.g., SEM studies (Marxen et al., 2008; Starborg et al., 2019).

4.2. Segmentation methods for determining porosity

We evaluated several different segmentation methods including automated algorithms in *Fiji*, such as *Otsu*, *Huang*, *Yen*, and *MaxEntropy*, which are widely accepted in different studies. All these algorithms overestimated the porosity and therefore were not suitable for our data and needs. Also, finding one single manually selected threshold value for both the SRμCT and BSE images was problematic, and no single value proved to be applicable in all the images. The peak width for the pore spaces of the SRμCT image was frequently larger than that of the BSE image, which results from the poorer contrast resolution of the SRμCT image (Tsuchiyama et al., 2005). A manually selected threshold value was applicable only to the BSE mosaic. Our search for a suitable segmenting method led to *TWS*, which we applied to train an algorithm using SRμCT slices to automatically segment the SRμCT and SEM data of

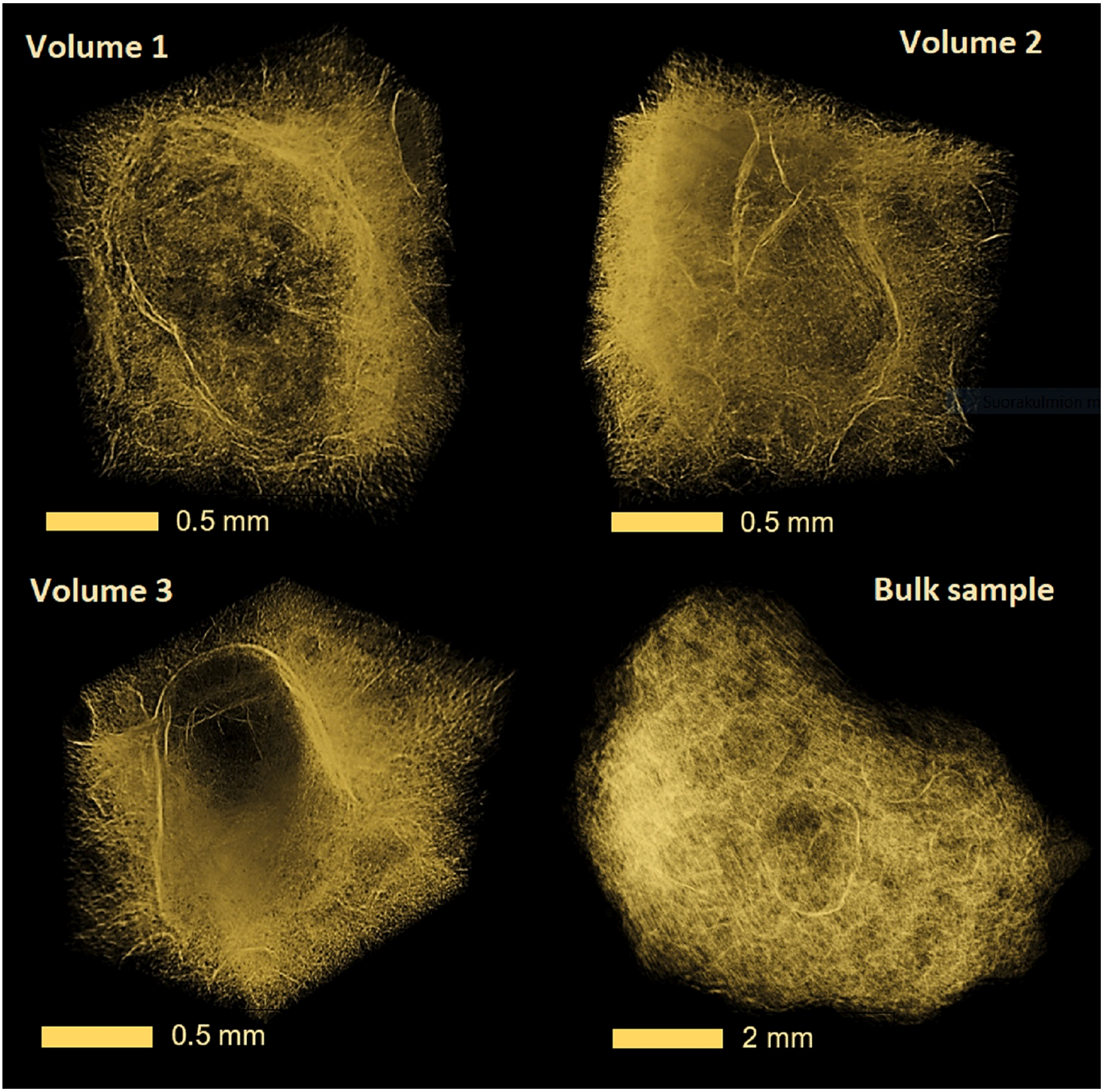

Fig. 6. 3D porosity renderings of Volume 1, Volume 2, and Volume 3 imaged using high-resolution SRμCT, and the bulk sample imaged using low-resolution SRμCT.

Areas 1–3. Thus, *TWS* allowed segmenting data of similar pixel size regardless of the imaging technique, and because the characteristics of Bjurböle are extreme among chondrites, this method applies to chondrites in general. Since computing feature vectors and random forest predictions from the feature vectors requires substantial computational resources, we turned to *Labkit* to segment the 3D datasets. *Labkit* is optimized for big image data and can process large datasets of several gigabytes (Arzt et al., 2022).

4.3. Representativeness of the analyzed regions

As the porosity in Bjurböle is heterogeneously distributed, small sample size may not be representative of the meteorite and image analyses may produce uncharacteristic results. Porosity variations increase with decreasing image size, i.e., the field of view, which is a result of the uneven distribution of voids. The area of the studied 2D images and the volume of the 3D stacks exceed the calculated REA and REV of ~1.4 mm^2 and ~ 1.9 mm^3, respectively, and the image analysis results are comparable to the 21.9 vol% porosity of the sample measured using a pycnometer. Thus, we conclude that the analyzed areas/volumes are representative of the sample on the macroscopic scale. Also, previously measured porosities of Bjurböle samples of approximately 20% (e.g., Kohout et al., 2017; Macke, 2010) agree with our results.

4.4. Porosity types

Bjurböle is an equilibrated and highly porous OC. The 2D and 3D results of the Bjurböle sample in this study show that most of the

Table 2
3D measurement results of pore properties of the bulk sample imaged using low-resolution SRμCT and Volumes 1–3 imaged using high-resolution SRμCT. The bulk porosity of the sample measured using pycnometry is included in the Table.

	Bulk sample pycnometer	Bulk sample LR SRμCT	Volume 1 HR SRμCT	Volume 2 HR SRμCT	Volume 3 HR SRμCT
Porosity [%]	21.9	16.2	18.5	24.3	23.0
Voxel side length [μm]		6.5	0.65	0.65	0.65
Number of pores		100,429	144,525	127,772	119,743
Max pore volume [μm^3]		53,985,776,733	552,657,397	613,360,279	572,110,587
Min pore volume [μm^3]		824	0.82	0.82	0.82
Mean pore volume [μm^3]		564,706	3978	4881	4949
SD of pore volume [μm^3]		170,353,024	1,452,646	1,715,923	1,653,312
Max Feret diameter [μm]		12,430	2533	2370	2376
Min Feret diameter [μm]		15.9	1.6	1.6	1.6
Mean Feret diameter [μm]		51.0	8.0	6.2	8.7
SD of Feret diameter [μm]		61.0	11.3	9.8	11.8
Max aspect ratio		16.6	15.3	16.1	18.6
Min aspect ratio		1.2	1.2	1.2	1.2
Mean aspect ratio		2.4	2.6	2.8	2.7
SD of aspect ratio		0.8	1.0	1.0	1.1

porosity resides in the intergranular pore space as interconnected network, whereas intragranular voids and cracks represent a negligible portion of the total porosity volume (Fig. 13).

In Bjurböle, gaps often separate chondrules and large mineral grains from the matrix. Cracks are present within chondrules, metal and mineral grains, as well as the matrix, and some of them are partially filled. Some chondrules and grains display chains and swarms of isolated pores. Few of the isolated pores in olivine and pyroxene grains are connected by intergrain cracks. Isolated tiny pores are present in metal grains as well, and they often appear more spherical and regular shaped. Some mineral laths are separated by gaps or low-density regions. In the following sections, we discuss the quantitative porosity properties.

4.5. Void size distributions

The ranges of void diameter and area show variations in the analyzed 2D regions. Mean void areas show differences between Areas 1–3, but the mean void diameter appears to be quite similar. The differences in the results of SEM and SRμCT may reflect the finite resolution of imaging, especially SRμCT, and the slightly different slice chosen. Areas 1 and 2 show a broader range of void diameter, which may be explained by large chondrules in their field of view that are surrounded by gaps.

The range of void diameter in Volumes 1–3 is similar. This range appears similar to the range of void diameters that represent nearly all the voids in the bulk sample and in the polished section. Both 2D and 3D results demonstrate that >90% of the voids are smaller in diameter than 50 μm. The presence of a large chondrule may explain the broader range of void diameter in Volume 1 compared to Volumes 2 and 3. The range of void volumes is similar in Volumes 1–3.

3D porosity results show most of the total void space volume resides in one continuous network of voids, i.e., pore space that includes gaps separating chondrules from the matrix and a complex structure in the matrix. The highest portion of the void spaces represents voids isolated from the largest pore space component and they are present within chondrules and matrix. Considering both 2D and 3D results of void diameter, area, and volume, small voids represent a higher percentage of all the void spaces.

4.6. Aspect ratio of pores

Ordinary chondrites demonstrate two types of porosity, that is, localized and continuous (e.g., Flynn et al., 1999; Friedrich et al., 2008). Continuous porosity blocks thermal paths but provides paths for shock propagation and thus influences the thermal properties and shock effects in meteorites and their parent bodies. In the investigated Bjurböle volumes, continuous porosity comprises over 95% of the total porosity (Fig. 13). Aspect ratio is linked to the interconnectivity and tortuosity of the void spaces, which in turn govern permeability and thus is an important parameter in the characterization of these properties (Soini et al., 2020). However, limited experimental data exist on aspect ratios of voids of meteorites.

The dominant void shape is circular in all the 2D data. Although, the ranges of aspect ratios show differences in the 2D porosity results, they are all centered on a comparable aspect ratio. The polished section and the Areas 1–3 contain voids of which shapes range from almost spherical to crack-like and include all shapes in between. The range of aspect ratios is consistently larger in SRμCT slices than in the respective BSE images (Supplementary Fig. 4), which may be due to the pixel sizes and the related differences in the interpretation of connected void spaces during segmentation as well as bleeding due to the lower contrast in SRμCT images.

The polished section contains the broadest range of aspect ratios of all the 2D and 3D analysis results. This may be explained by the stereological principle in SEM analysis assuming a model shape. 3D SRμCT estimation should be closer to the truth and produce more representative results as the 3D analysis does not require such assumptions on the void shapes (Peyrin et al., 2007).

Between the investigated volumes, the range of aspect ratio is broadest in Volume 3. The range is quite similar in the bulk sample volume and its subvolumes despite the voxel side length difference between high- and low-resolution measurements. Spherical voids represent the highest percentage of the void spaces in all the volumes. High aspect ratios represent a small fraction of the total porosity in all the investigated areas/volumes, but they may have a significant effect on, e.g., thermal properties. For example, Opeil et al. (2012) and Soini et al. (2020) reported differences in thermal conductivities of meteorites depending on the measurement direction, which exceed any measurement error. Elongated voids and cracks cause heterogeneity and structural variation in thermal conductivity and thus possibly anisotropy. Fig. 14 shows a porosity model considering anisotropy of Volume 3 in Bjurböle.

A weakly positive correlation between aspect ratio of voids and void diameter is present in SRμCT slices of Areas 1–3, BSE image of Area 3, and in the polished section. In Volumes 1–3 and the bulk sample, the linear relationship between aspect ratio of voids and void diameter is moderately positive. The positive correlation is stronger in the 3D results, which is likely due to the stereological bias associated to SEM. Thus, larger voids tend to have higher aspect ratios. Note that the plots of the relationship between aspect ratio and void diameter of the 2D polished section and the 3D results are calculated from resampled data, where evenly spaced diameter values and mean of aspect ratio are used to visualize the large datasets with >100,000 data points. Feret

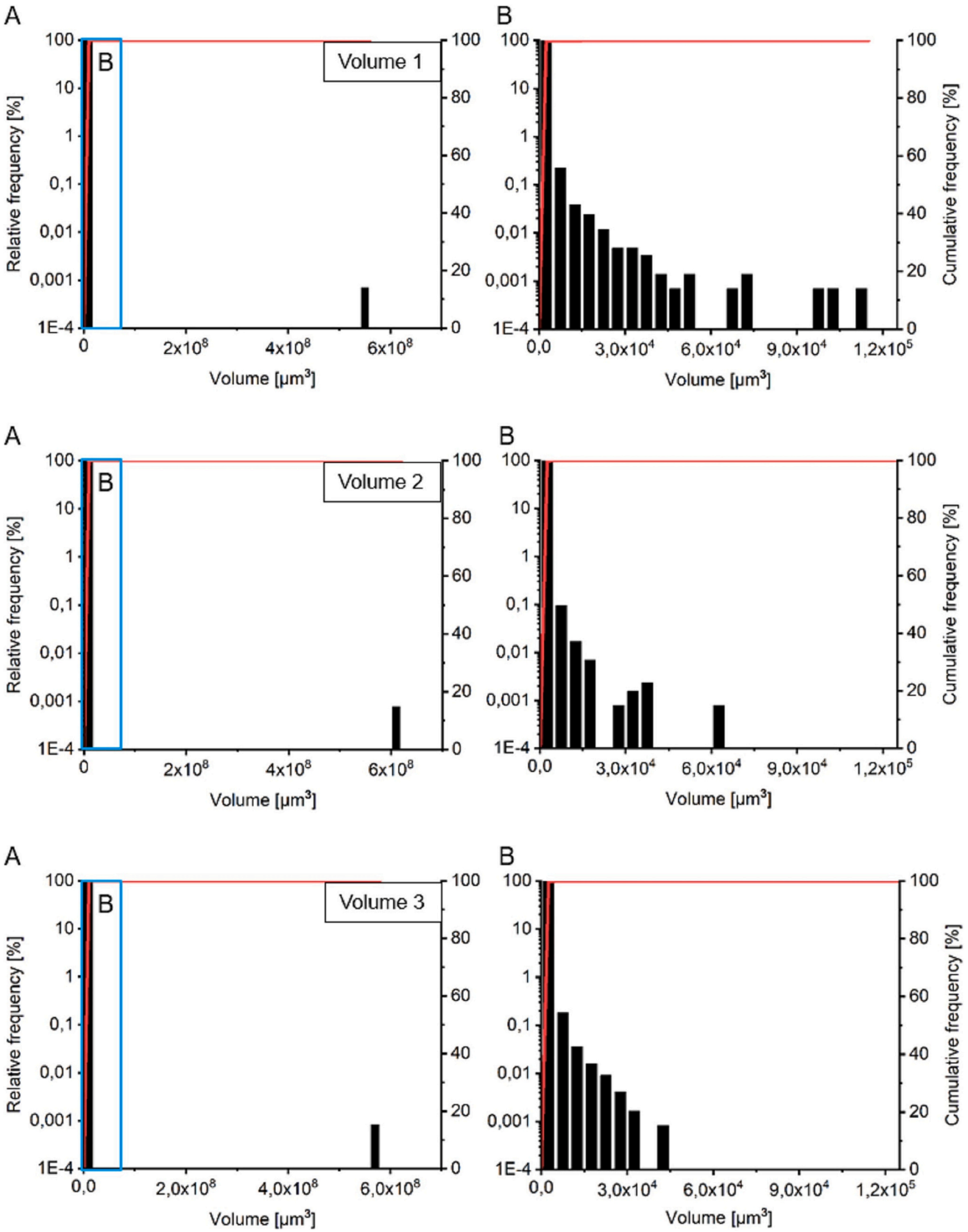

Fig. 7. Void volume distribution of Volumes 1–3 imaged using high-resolution SRμCT. Plot A shows the entire range of void volumes and plot B shows the detailed distribution of the void volumes defined with the blue box that have high relative frequency. The red line represents the cumulative frequency. (For interpretation of the references to colour in this figure legend, the reader is referred to the web version of this article.)

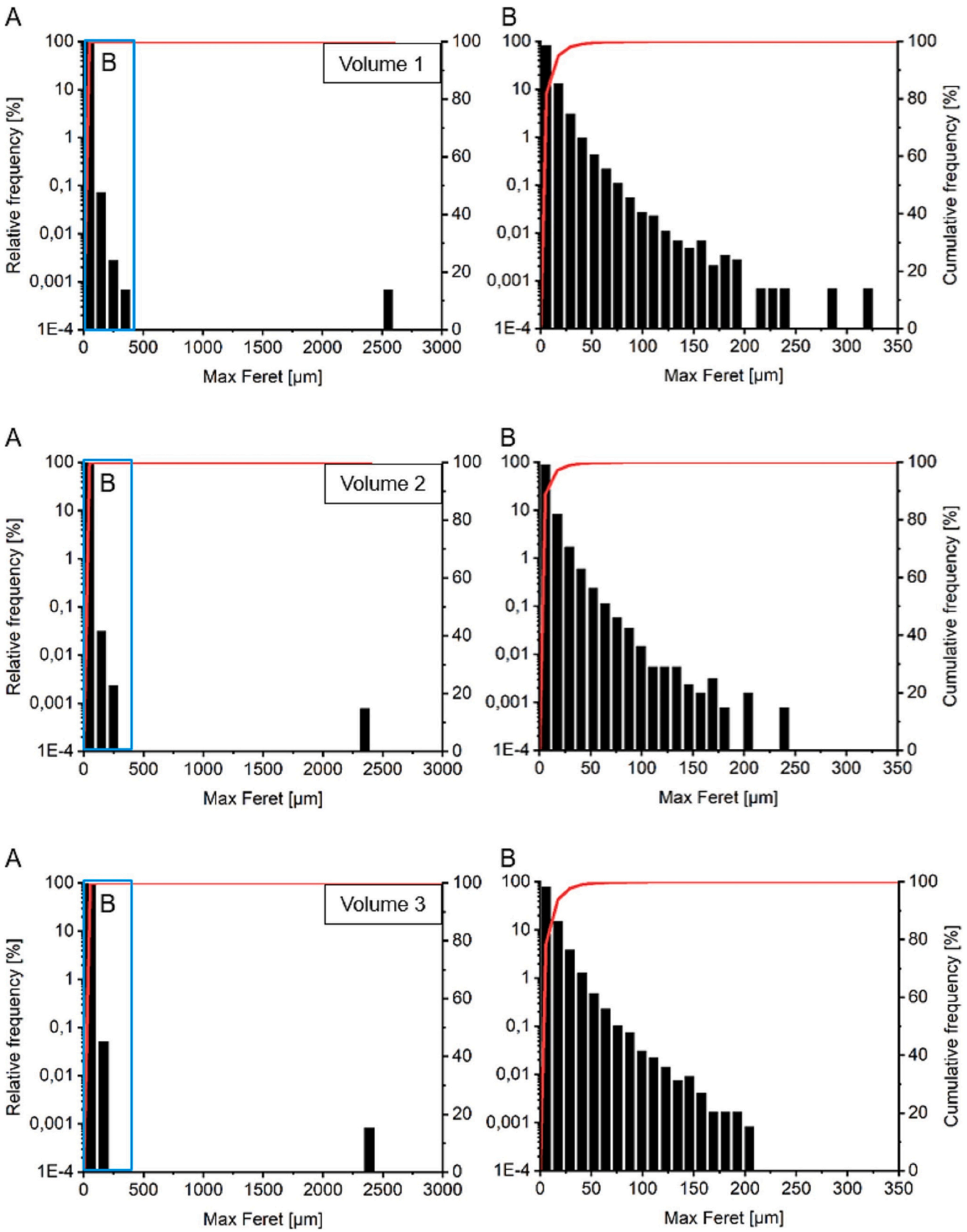

Fig. 8. Maximum Feret diameter distribution of Volumes 1–3 imaged using high-resolution SRμCT. Maximum Feret diameter represents the void diameter. See section 2.4.2 for detailed definition of maximum Feret diameter. Plot A shows the entire range of maximum Feret diameters and plot B shows the detailed distribution of the maximum Feret diameters defined with the blue box that have high relative frequency. The red line represents the cumulative frequency. (For interpretation of the references to colour in this figure legend, the reader is referred to the web version of this article.)

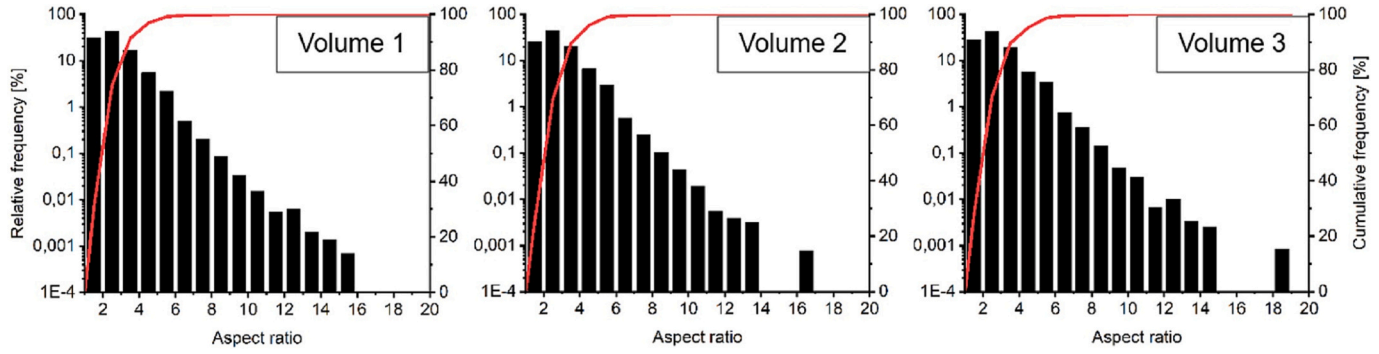

Fig. 9. Void aspect ratio distributions of Volumes 1–3 imaged using high-resolution SRμCT. The red line represents the cumulative frequency. (For interpretation of the references to colour in this figure legend, the reader is referred to the web version of this article.)

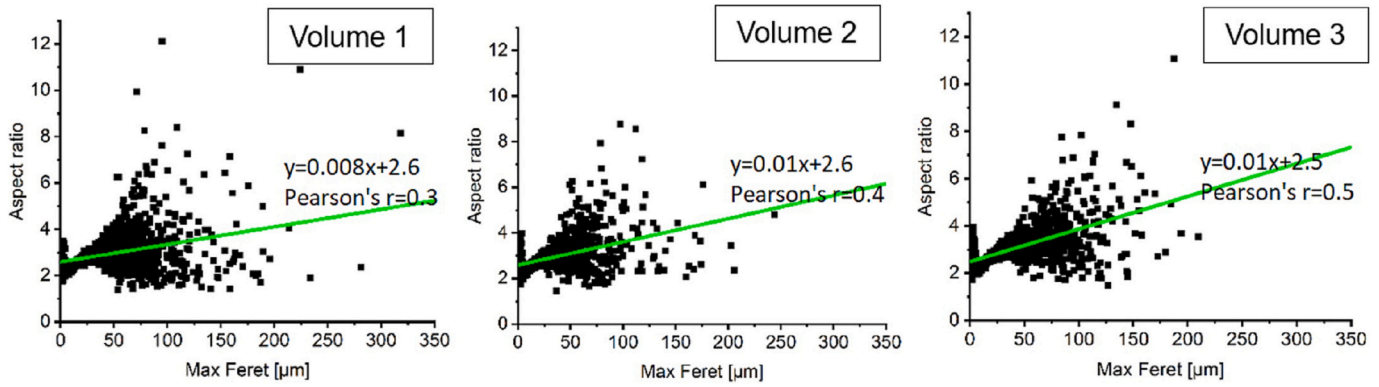

Fig. 10. The relationship between maximum Feret diameter and aspect ratio of voids in Volumes 1–3 imaged using high-resolution SRμCT. Maximum Feret diameter represents the void diameter. See section 2.4.2 for detailed definition of maximum Feret diameter. The data are calculated from resampled data using evenly spaced maximum Feret values and mean of the aspect ratio. The green line shows the positive correlation between maximum Feret diameter and aspect ratio. (For interpretation of the references to colour in this figure legend, the reader is referred to the web version of this article.)

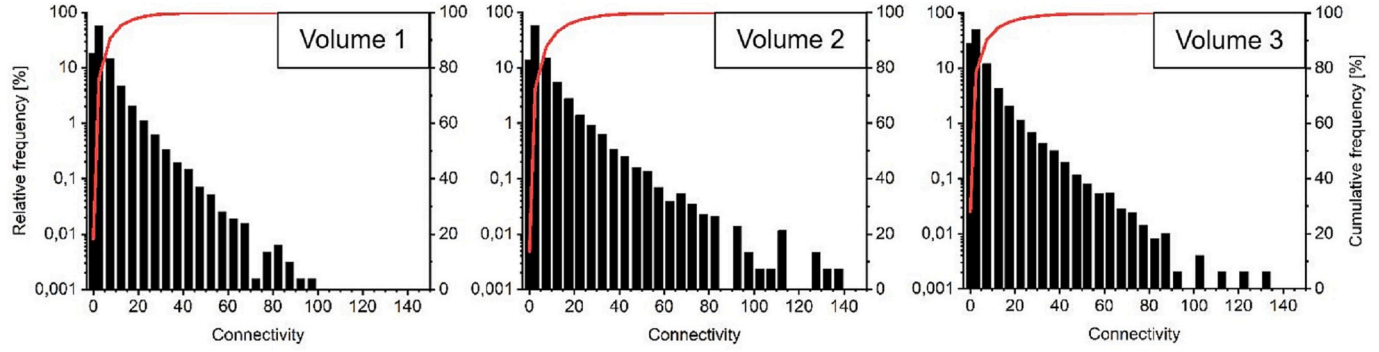

Fig. 11. Void connectivity distributions of Volumes 1–3 imaged using high-resolution SRμCT. The connectivity value represents the number of connections of the voids to other void spaces. The red line represents the cumulative frequency. (For interpretation of the references to colour in this figure legend, the reader is referred to the web version of this article.)

diameters, i.e., void diameters, are to some degree quantized to the available pore pixel sizes and arrangements. In other words, the number of possible values of void diameter is restricted so that certain voids can assume only certain discrete values. For example, the smallest voids do not represent every possible diameter and image analysis will undoubtedly lead to quantization where real-world values are estimated by digital representation, which unavoidably sets up limits on the precision and dimension of a value.

4.7. Void connectivity

Voids with fewer connections are more frequent than continuous void spaces that have tens or > 100 connections. Voids with 1–10 connections represent the highest percentage and completely isolated pores represent the second highest percentage of all the void spaces in the bulk sample and Volumes 1–3.

A very high positive correlation between void volume and connectivity in Volumes 1-3 is visible in Fig. 12 and large voids frequently have more connections to other void spaces compared to smaller voids. A strongly positive linear relationship is also present in the bulk sample

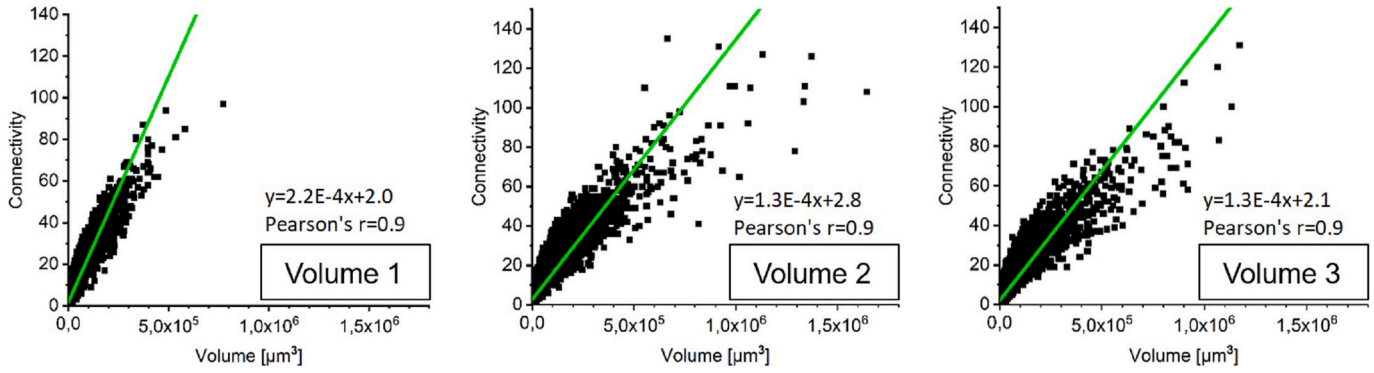

Fig. 12. The relationship between void volume and connectivity in Volumes 1–3 imaged using high-resolution SRµCT. The connectivity value represents the number of connections of the voids to other void spaces. The green line shows the positive correlation between void volume and connectivity. (For interpretation of the references to colour in this figure legend, the reader is referred to the web version of this article.)

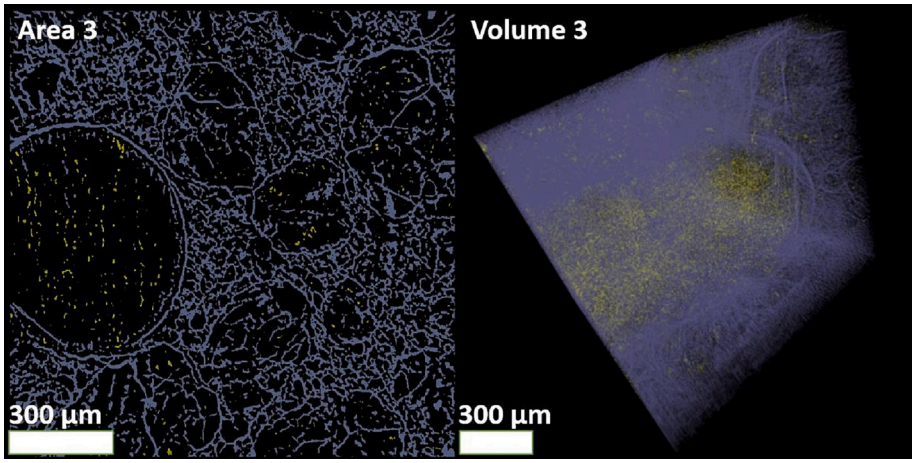

Fig. 13. Porosity components of Area 3 and respective Volume 3 in the Bjurböle sample. The largest continuous porosity component comprises almost all the void space and is shown in gray colour. The rest of the porosity components comprise a negligible portion of the void space despite representing tens of thousands of smaller voids and are shown in yellow colour. (For interpretation of the references to colour in this figure legend, the reader is referred to the web version of this article.)

and thus in all the 3D data. Volume 2 and 3 contain a higher ratio of matrix to chondrules, which may explain the larger void connectivity compared to Volume 1 in which a large chondrule occupies much of the volume. Voids in the matrix form complex networks with large connectivity and volume but low relative frequency and they are often connected to the gaps surrounding the chondrules. Positive correlations between void diameter and aspect ratio as well as void volume and connectivity indicate larger voids have higher aspect ratio and higher connectivity. Isolated pores within the chondrules and matrix are small in volume but represent a high portion of all the void spaces. Interconnectedness can only reliably be seen in 3D and disguised in 2D, and the volume fraction and the number of the interconnected components are important for understanding porosity in general.

4.8. Implications for the accretion and thermal evolution of Bjurböle

The results of the present study provide means to speculate the accretion and thermal evolution of Bjurböle. The small, isolated voids with small aspect ratio inside the chondrules in Areas 1–3 (Figs. 1, 3, and Supplementary Fig. 1) probably represent vesicles, i.e., primary porosity due to exsolution of gas from the chondrule melt during cooling (Lewis et al., 2018). Such voids are ubiquitously present within the chondrules, but they are also concentrated on the rims of the chondrules. Some of the intra-chondrule porosity, especially the linear chains of pores in Areas 1 and 2 (Supplementary Fig. 1) can be attributed to leaching of chondrule mesostasis in low temperature aqueous alteration (Lewis et al., 2018). Further, the internal cracks of the chondrules that do not extend to the matrix indicate collisions during the chondrule formation in the solar nebula or during accretion or re-accretion. Some of the chondrules are also fragments of original spherules. Practically all chondrules are surrounded by gaps, which we interpret as contraction effects during cooling of the parent body, or they may be due to low temperature after final accretion insufficient for complete lithification. The well-connected, intergranular pore space in the matrix suggests the matrix was not efficiently recrystallized (sintered) after final accretion.

Theoretical models of the thermal evolution of chondritic parent bodies including compaction ('cold pressing') and subsequent sintering at high temperatures suggest that porosity is strongly reduced in the process (Yomogida and Matsui, 1984; Henke et al., 2012). These models assume instantaneous accretion of the body a few Ma after the formation of the calcium-aluminum inclusions (Miyamoto et al., 1981; Miyamoto, 1991; Bennett III and McSween Jr., 1996; Yomogida and Matsui, 1984; Ghosh et al., 2003; Henke et al., 2012; Gail et al., 2015) and support an onion shell model for OC parent bodies. Thermal evolution models (e.g., Henke et al., 2012) suggest that the most rapid porosity change from 40 to 15% occurs at temperatures slightly above the onset of sintering (330–340 °C), and porosity is modeled to further decrease with increasing temperatures to ~10% at 530 °C. In the model of Henke et al. (2012), decreasing pore space reduces the initial 100-km-radius to the final radius of 85 km, which corresponds to the final radius of the body after compaction and practically zero porosity at all depths, in only 0.8 Ma after accretion. Porosities comparable to those measured in Bjurböle are present in onion-shell models only for a noticeably brief time after sintering begins. The petrologic type 4 of Bjurböle indicates peak metamorphic temperatures ranging from 600 to 700 °C, which should have led to a drastic reduction in porosity. Therefore, the observed high

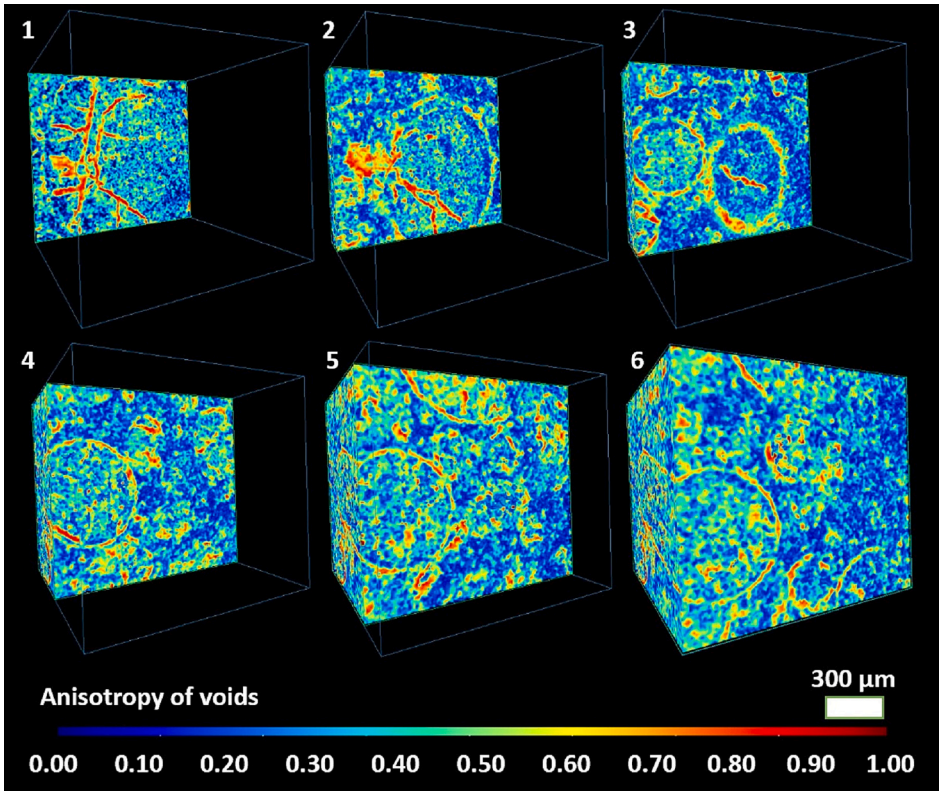

Fig. 14. A 3D model of anisotropy of porosity in Volume 3 of Bjurböle constructed using Bone Analysis module in Dragonfly software. The box in light blue colour shows the outlines of the total volume. From 1 to 6, the portion of the visible volume increases revealing different cross sections of the volume; illustration 1 shows the back wall of the volume, while illustration 6 shows the whole volume. Anisotropy increases from blue (0) to red colour (1). The degree of anisotropy is 0 for an isotropic system and increases as the system becomes more anisotropic. (For interpretation of the references to colour in this figure legend, the reader is referred to the web version of this article.)

porosity of Bjurböle cannot be interpreted with a simple onion shell model. Instead, it suggests Bjurböle represents a fragment of a body disintegrated during its metamorphic evolution. It remains an open question how Bjurböle demonstrates such high metamorphic temperatures. One option could be that the parent body was already substantially heated during accretion (Ghosh et al., 2003). Accretion time is a controlling factor of the peak temperature the body experiences and the accretion of the parent body of Bjurböle may have lasted a long time after which the body disintegrated.

According to thermal models including compaction and sintering, the porosity of chondrites should decrease with increasing metamorphic grade. However, this is not observed in studies of Bjurböle or other chondrites (e.g., Wilkison et al., 2003; Sasso et al., 2009; Soini et al., 2020). Several thermal, chronologic, and petrographic studies (e.g., Scott et al., 2014; Ganguly et al., 2013, 2016; Blackburn et al., 2017; Bischoff et al., 2018) support the fragmentation-reassembly model introduced among the first by Grimm (1985) and Taylor et al. (1987) to explain the thermal evolution of OC parent bodies. The thermal evolution model of Lucas et al. (2020) incorporates fragmentation of an initial onion shell body at peak or near-peak temperatures and rapid reassembly into a thermally stable rubble pile. Metasomatism and aqueous alteration during thermal metamorphism affect the evolution of porosity in the OC parent body (Lewis et al., 2018). Rubble pile structures are further supported with evidence of low densities measured for S-type asteroids such as 25143 Itokawa (Carry, 2012) compared to meteorites (e.g., Consolmagno et al., 2008), which indicates high porosities for asteroid parent bodies relative to compact, unfractured rock (Lucas et al., 2020).

Our results support the previous measurements of high-porosity chondrites and rubble pile structure suggested for their parent body (e.g., Sasso et al., 2009; Friedrich et al., 2008). The high porosity chondrites including Bjurböle may be attributed to impact-induced brecciation during or after metamorphism in a fragmentation-reassembly process (Lucas et al., 2020). Thus, Bjurböle may sample a parent body that was rapidly reaccreted after the fragmentation of the initial onion shell body (or bodies) at high temperatures. Chondrites have complex thermal histories in which porosity plays a vital role, and advances in modeling are required to survey the different possible scenarios. For example, current thermal models have treated the aspect ratios of void spaces as unknown quantities, i.e., as free parameters due to the lack of measurement data (Gail and Trieloff, 2018). This study adds to the previous measurements by providing novel three-dimensional quantitative results of the geometry and connectivity of porosity that can be used to develop the thermal models of OC parent bodies.

5. Conclusions

We applied SRµCT and SEM at sub-micron resolution to characterize the porosity of L/LL4 ordinary chondrite Bjurböle in 2D and 3D. *Trainable Weka Segmentation* is a convenient tool to automatically segment data of comparable pixel size obtained using SRµCT and SEM. *Labkit* is efficient in automated segmentation of large SRµCT datasets. These tools combine visual qualitative examination and machine learning algorithms that can be applied to both SRµCT and SEM data to obtain satisfactory segmentation results for the porosity analyses. At similar resolution, SRµCT and SEM produce comparable 2D results. Although higher resolution can be reached with SEM, it causes stereological bias. When comparing the 2D and 3D results, the effect of this bias was especially obvious in the results of the aspect ratios of voids. 3D SRµCT eliminates this concern and should produce an estimation that is closer to the truth. The comparison between SRµCT and SEM led to the conclusion that they are powerful as standalone tools as well as supplementary tools to add to other studies allowing more complete and detailed investigations of porosity. Because the characteristics of Bjurböle are exceptional among chondrites, these means can be applied to chondrites in general to achieve credible results of their porosity properties.

The Bjurböle sample in this study is a complex, highly porous, and friable medium. Imaging reveals the heterogeneous distribution of

porosity, and its dominant type is intergranular continuous porosity. Almost all porosity volume resides in one connected component, which contains a complex network of void spaces within the matrix often connected to the gaps surrounding the chondrules. Continuous porosity has a significant effect on thermal properties, e.g., the effectiveness of thermal conduction, in meteorites and their parent bodies. Thus, the aspect ratios of voids, which are linked to the interconnectivity of voids, represent an important parameter in the characterization of thermal properties.

2D and 3D results show weakly or moderately positive linear relationships between aspect ratio of voids and void diameter indicating smaller voids are more spherical. Additionally, 3D results reveal a very high positive correlation between connectivity and void volume indicating smaller voids have fewer connections to other void spaces. Thus, these relationships suggest smaller voids have lower aspect ratios and lower connectivity. In the Bjurböle sample of this study, small voids with 1–10 connections have the highest relative frequency, whereas larger void spaces with higher aspect ratios and connectivity are significantly fewer. Completely isolated pores have the second highest relative frequency, and they exist within the chondrules and the matrix. However, the volume percentage of these pores is negligible compared to the continuous pore space. The volume percentage of intergranular void spaces and the low shock stage of Bjurböle suggest accretion with little compaction. This intergranular porosity in Bjurböle may describe some degree of intrinsic accretionary yet sintered and metamorphosed material.

Our results show high porosity in Bjurböle and agree with the previous measurements of high-porosity chondrites. We note that the high porosity and its heterogeneous distribution are not in line with the thermal evolution and sintering models of chondritic parent bodies regarding petrologic type 4. Therefore, Bjurböle may originate from a parent body with an initial onion shell structure that fragmented during or after its metamorphic peak and quickly reaccreted into a rubble pile.

Porosity is an important parameter in the thermal models of ordinary chondrite parent bodies. The aspect ratios of void spaces have been treated as free parameters due to the lack of measurement results. This study adds to the previous studies of chondrite porosity by providing novel three-dimensional quantitative results of void geometry and connectivity that can be used to advance the thermal models of OC parent bodies.

Funding

This work was supported by the Vilho, Yrjö, and the Kalle Väisälä Foundation of Finnish Academy of Science and Letters, Nordenskiöld-Samfundet, Academy of Finland project no. 335595, NASA SSERVI Center for Lunar and Asteroid Surface Science (CLASS), and within institutional support RVO 67985831 of the Institute of Geology of the Czech Academy of Sciences.

CRediT authorship contribution statement

A.-J. Soini: Conceptualization, Methodology, Software, Formal analysis, Investigation, Writing – original draft, Visualization, Funding acquisition. **I.T. Kukkonen:** Conceptualization, Resources, Writing – review & editing, Supervision. **H. Suhonen:** Conceptualization, Methodology, Software, Investigation, Writing – review & editing. **B. Lukić:** Methodology, Investigation, Resources, Data curation, Writing – review & editing. **T. Kohout:** Writing – review & editing, Supervision. **A.V. Luttinen:** Resources, Writing – review & editing, Supervision.

Declaration of Competing Interest

The authors declare that they have no known competing financial interests or personal relationships that could have appeared to influence the work reported in this paper.

Data availability

SRμCT datasets related to this article can be found at doi.org/10.15151/ESRF-DC-1163775534 (Soini et al. 2023), an online data repository hosted at ESRF. BSE images and elemental maps that support the findings of this work are openly available at https://doi.org/10.5281/zenodo.6504816 (Soini et al. 2022), an online data repository hosted at Zenodo.

Acknowledgments

We thank Dominik Hezel and an anonymous reviewer for critically reviewing the manuscript and proposing valuable improvements. *We acknowledge the European Synchrotron Radiation Facility for the provision of synchrotron radiation facilities, and we would like to thank* Ludovic Broche and *Alexander Rack for their assistance in using beamline ID19. We would also like to thank Katie Doig and Adam Abersteiner for their help in preparing the polished section and for constructive discussions and assistance on the SEM.* This is publication #0009 of the Geophysical, environmental, and mineralogical laboratories (HelLabs) of the University of Helsinki.

Appendix A. Supplementary data

Supplementary material that contains the plots of the 2D porosity results of SRμCT and corresponding BSE images at comparable resolution as well as the plots of the 3D porosity results of the bulk sample scanned at low-resolution SRμCT can be found in the online version of this article.

References

Allaby, M., 2020. A Dictionary of Geology and Earth Sciences, 5th ed. Oxford University Press, Oxfrod.

Andre, S.L., McCoy, T.J., McCamant, J.E., Robinson, M.S., Britt, D.T., 2003. Densities and Porosities of Ordinary Chondrites; Do High Porosity Meteorites Represent Regolith Materials? Lunar and Planetary Science Conference XXXIV, Abstract #1608.

Arganda-Carreras, I., Kaynig, V., Rueden, C., Eliceiri, K.W., Schindelin, J., Cardona, A., Sebastian Seung, H., 2017. Trainable Weka Segmentation: a machine learning tool for microscopy pixel classification. Bioinformatics 33 (15), 2424–2426. https://doi.org/10.1093/bioinformatics/btx180.

Arzt, M., Deschamps, J., Schmied, C., Pietzsch, T., Schmidt, D., Tomancak, P., Haase, R., Jug, F., 2022. LABKIT: labeling and segmentation toolkit for big image data. Front. Comput. Sci. 4 https://doi.org/10.3389/fcomp.2022.777728.

Bartyzel, K., 2016. Adaptive Kuwahara filter. Signal Image Video Process 10 (4), 663–670. https://doi.org/10.1007/s11760-015-0791-3.

Bennett III, M.E., McSween Jr., H.Y., 1996. Revised model calculations for the thermal histories of ordinary chondrite parent bodies. Meteorit. Planet. Sci. 31 (6), 783–792. https://doi.org/10.1111/j.1945-5100.1996.tb02113.x.

Bischoff, A., Schleiting, M., Wieler, R., Patzek, M., 2018. Brecciation among 2280 ordinary chondrites–constraints on the evolution of their parent bodies. Geochim. Cosmochim. Acta 238, 516–541. https://doi.org/10.1016/j.gca.2018.07.020.

Biswas, S., Ghoshal, D., 2016. Blood cell detection using thresholding estimation based watershed transformation with Sobel filter in frequency domain. Proc. Comput. Sci. 89, 651–657. https://doi.org/10.1016/j.procs.2016.06.029.

Blackburn, T., Alexander, C.M.D., Carlson, R., Elkins-Tanton, L.T., 2017. The accretion and impact history of the ordinary chondrite parent bodies. Geochim. Cosmochim. Acta 200, 201–217. https://doi.org/10.1016/j.gca.2016.11.038.

Bryson, J.F., Neufeld, J.A., Nimmo, F., 2019. Constraints on asteroid magnetic field evolution and the radii of meteorite parent bodies from thermal modelling. Earth Planet. Sci. Lett. 521, 68–78. https://doi.org/10.1016/j.epsl.2019.05.046.

Carry, B., 2012. Density of asteroids. Planet. Space Sci. 73 (1), 98–118. https://doi.org/10.1016/j.pss.2012.03.009.

Chang, S.Y., Morgan, N., 2014. Robust CNN-based speech recognition with Gabor filter kernels. In: Proceedings of the Annual Conference of the International Speech Communication Association, INTERSPEECH.

Consolmagno, G.J., Britt, D.T., 1998. The density and porosity of meteorites from the Vatican collection. Meteorit. Planet. Sci. 33, 1231–1241. https://doi.org/10.1111/j.1945-5100.1998.tb01308.x.

Consolmagno, G.J., Britt, D.T., Macke, R.J., 2008. The significance of meteorite density and porosity. Geochemistry 68 (1), 1–29. https://doi.org/10.1016/j.chemer.2008.01.003.

CTC, 2021. Available online at: http://celltrackingchallenge.net/latest-csb-results (accessed March 23, 2023).

Drugan, W.J., Willis, J.R., 1996. A micromechanics-based nonlocal constitutive equation and estimates of representative volume element size for elastic composites. J. Mech. Phys. Solids 44, 497–524. https://doi.org/10.1016/0022-5096(96)00007-5.
Dubetz, D.A., 2016. Micro-CT Characterization of Pore-Size Distribution and Effects on Matrix Acidizing (Master of Science Thesis). Texas A&M University.
Ebel, D.S., Rivers, M.L., 2007. Meteorite 3-D synchrotron microtomography: methods and applications. Meteorit. Planet. Sci. 42 (9), 1627–1646. https://doi.org/10.1111/j.1945-5100.2007.tb00595.x.
Edwards, G.H., Blackburn, T., 2020. Accretion of a large LL parent planetesimal from a recently formed chondrule population. Sci. Adv. 6 (16) https://doi.org/10.1126/sciadv.aay8641 eaay8641.
Farbaniec, L., Chapman, D.J., Patten, J.R., Smith, L.C., Hogan, J.D., Rack, A., Eakins, D. E., 2021. In-situ visualisation of dynamic fracture and fragmentation of an L-type ordinary chondrite by combined synchrotron X-ray radiography and microtomography. Icarus 359, 114346. https://doi.org/10.1016/j.icarus.2021.114346.
Florin, G., Luais, B., Rushmer, T., Alard, O., 2020. Influence of redox processes on the germanium isotopic composition of ordinary chondrites. Geochim. Cosmochim. Acta 269, 270–291. https://doi.org/10.1016/j.gca.2019.10.038.
Flynn, G.J., Moore, L.B., Klöck, W., 1999. Density and porosity of stone meteorites: implications for the density, porosity, cratering, and collisional disruption of asteroids. Icarus 142, 97–105. https://doi.org/10.1006/icar.1999.6210.
Flynn, G.J., Consolmagno, G.J., Brown, P., Macke, R.J., 2018. Physical properties of the stone meteorites: implications for the properties of their parent bodies. Geochemistry 78 (3), 269–298. https://doi.org/10.1016/j.chemer.2017.04.002.
Francis, J.J., De Jager, G., 2005. The bilateral median filter. SAIEE Afr Res J. 96, 106–111. https://doi.org/10.23919/SAIEE.2005.9488092.
Friedrich, J.M., Rivers, M.L., 2013. Three-dimensional imaging of ordinary chondrite microporosity at 2.6 μm resolution. Geochim. Cosmochim. Acta 116, 63–70. https://doi.org/10.1016/j.gca.2011.08.045.
Friedrich, J.M., Macke, R.J., Wignarajah, D.P., Rivers, M.L., Britt, D.T., Ebel, D.S., 2008. Pore size distribution in an uncompacted equilibrated ordinary chondrite. Planet. Space Sci. 56 (7), 895–900. https://doi.org/10.1016/j.pss.2008.02.002.
Friedrich, J.M., Wignarajah, D.P., Chaudhary, S., Rivers, M.L., Nehru, C.E., Ebel, D.S., 2008b. Three-dimensional petrography of metal phases in equilibrated L chondrites—effects of shock loading and dynamic compaction. Earth Planet. Sci. Lett. 275 (1–2), 172–180. https://doi.org/10.1016/j.epsl.2008.08.024.
Friedrich, J.M., Chen, M.M., Giordano, S.A., Matalka, O.K., Strasser, J.W., Tamucci, K.A., Rivers, M.L., Ebel, D.S., 2021. Size-frequency distributions and physical properties of chondrules from x-ray computed microtomography and digital data extraction. Microsc. Res. Tech. 1–11 https://doi.org/10.1002/jemt.24043.
Gail, H.P., Trieloff, M., 2018. Thermal evolution and sintering of chondritic planetesimals IV. Temperature dependence of heat conductivity of asteroids and meteorites. Astron. Astrophys. 615, A147. https://doi.org/10.1051/0004-6361/201732456.
Gail, H.P., Henke, S., Trieloff, M., 2015. Thermal evolution and sintering of chondritic planetesimals II. Improved treatment of the compaction process. Astron. Astrophys. 576, A60. https://doi.org/10.1051/0004-6361/201424278.
Galli, M., Cugnoni, J., Botsis, J., 2012. Numerical and statistical estimates of the representative volume element of elastoplastic random composites. Eur. J. Mech. A Solid. 33, 31–38. https://doi.org/10.1016/j.euromechsol.2011.07.010.
Ganguly, J., Tirone, M., Chakraborty, S., Domanik, K., 2013. H chondrite parent asteroid: a multistage cooling, fragmentation and re-accretion history constrained by thermometric studies, diffusion kinetic modeling and geochronological data. Geochim. Cosmochim. Acta 105, 206–220. https://doi.org/10.1016/j.gca.2012.11.024.
Ganguly, J., Tirone, M., Domanik, K., 2016. Cooling rates of LL, L, and H chondrites and constraints on the duration of peak thermal conditions: diffusion kinetic modeling and implications for fragmentation of asteroids and impact resetting of petrologic types. Geochim. Cosmochim. Acta 192, 135–148. https://doi.org/10.1016/j.gca.2016.07.030.
Ghosh, A., Weidenschilling, S.J., McSween Jr., H.Y., 2003. Importance of the accretion process in asteroid thermal evolution: 6 Hebe as an example. Meteorit. Planet. Sci. 38 (5), 711–724. https://doi.org/10.1111/j.1945-5100.2003.tb00036.x.
Ginat, D.T., Gupta, R., 2015. Computed tomography. In: Peh, W. (Ed.), Pitfalls in Diagnostic Radiology. Springer, Berlin, Heidelberg. https://doi.org/10.1007/978-3-662-44169-5_2.
GitLab, 2022. tomotools / Nabu. https://gitlab.esrf.fr/tomotools/nabu. Accessed 27 April 2022.
Gostick, J., Aghighi, M., Hinebaugh, J., Tranter, T., Hoeh, M.A., Day, H., Spellacy, B., Sharqawy, M.H., Bazylak, A., Burns, A., Lehnert, W., 2016. OpenPNM: a pore network modeling package. Comput. Sci. Eng. 18 (4), 60–74. https://doi.org/10.1109/MCSE.2016.49.
Gostick, J.T., Khan, Z.A., Tranter, T.G., Kok, M.D., Agnaou, M., Sadeghi, M., Jervis, R., 2019. PoreSpy: a Python toolkit for quantitative analysis of porous media images. J. Open Source Softw. 4 (37), 1296. https://doi.org/10.21105/joss.01296.
Grady, M.M., 2000. Catalogue of Meteorites, 5th edition. Cambridge Univ. Press, Edinburgh, UK.
Grimm, R.E., 1985. Penecontemporaneous metamorphism, fragmentation, and reassembly of ordinary chondrite parent bodies. J. Geophys. Res. 90, 2022–2028. https://doi.org/10.1029/JB090IB02P02022.
Haase, R., Royer, L.A., Steinbach, P., Schmidt, D., Dibrov, A., Schmidt, U., et al., 2020. Clij: Gpu-accelerated image processing for everyone. Nat. Methods 17, 5–6. https://doi.org/10.1038/s41592-019-0650-1.
Hall, M., Frank, E., Holmes, G., Pfahringer, B., Reutemann, P., Witten, I.H., 2009. The WEKA data mining software: an update. ACM SIGKDD Explorat. Newslett. 11 (1), 10–18. https://doi.org/10.1145/1656274.1656278.
Hanna, R.D., Ketcham, R.A., 2017. X-ray computed tomography of planetary materials: a primer and review of recent studies. Chem. Erde 77, 547–572. https://doi.org/10.1016/j.chemer.2017.01.006.
Harrison, K.P., Grimm, R.E., 2010. Thermal constraints on the early history of the H-chondrite parent body reconsidered. Geochim. Cosmochim. Acta 74 (18), 5410–5423. https://doi.org/10.1016/j.gca.2010.05.034.
Hellmann, J.L., Kruijer, T.S., Van Orman, J.A., Metzler, K., Kleine, T., 2019. Hf-W chronology of ordinary chondrites. Geochim. Cosmochim. Acta 258, 290–309. https://doi.org/10.1016/j.gca.2019.05.040.
Henke, S., Gail, H.P., Trieloff, M., Schwarz, W.H., Kleine, T., 2012. Thermal history modelling of the H chondrite parent body. Astron. Astrophys. 545, A135. https://doi.org/10.1051/0004-6361/201219100.
Hezel, D.C., Elangovan, P., Viehmann, S., Howard, L., Abel, R.L., Armstrong, R., 2013. Visualisation and quantification of CV chondrite petrography using micro-tomography. Geochim. Cosmochim. Acta 116, 33–40.
Jones, R.H., 2003. Meteorites. In: Meyers, R.A. (Ed.), Encyclopedia of Physical Science and Technology, 3rd edition. Academic Press, pp. 559–574.
Ketcham, R.A., Hildebrandt, J., 2014. Characterizing, measuring, and utilizing the resolution of CT imagery for improved quantification of fine-scale features. Nucl. Instrum. Methods Phys. Res. Sect. B 324, 80–87. https://doi.org/10.1016/j.nimb.2013.08.064 (2014).
Kohout, T., Soini, A.-J., Yakovlev, G.A., Kruglikov, N.A., Luttinen, A., Grokhovsky, V.I., 2017. Distribution of Strength and Porosity in Small Asteroids, Lunar and Planetary Science Conference XLVIII, Abstract #2778.
Kuva, J., Sammaljärvi, J., Parkkonen, J., Siitari-Kauppi, M., Lehtonen, M., Turpeinen, T., Timonen, J., Voutilainen, M., 2018. Imaging connected porosity of crystalline rock by contrast agent-aided X-ray microtomography and scanning electron microscopy. J. Microsc. 270 (1), 98–109. https://doi.org/10.1111/jmi.12661.
Lewis, J.A., Jones, R.H., Garcea, S.C., 2018. Chondrule porosity in the L4 chondrite Saratov: dissolution, chemical transport, and fluid flow. Geochim. Cosmochim. Acta 240, 293–313. https://doi.org/10.1016/j.gca.2018.08.002.
Limaye, A., 2012. Drishti: A volume exploration and presentation tool. In: Developments in X-Ray Tomography VIII, Vol. 8506. International Society for Optics and Photonics, p. 85060X. https://doi.org/10.1117/12.935640.
Lucas, M.P., Dygert, N., Ren, J., Hesse, M.A., Miller, N.R., McSween, H.Y., 2020. Evidence for early fragmentation-reassembly of ordinary chondrite (H, L, and LL) parent bodies from REE-in-two-pyroxene thermometry. Geochim. Cosmochim. Acta 290, 366–390. https://doi.org/10.1016/j.gca.2020.09.010.
Macke, R.J., 2010. Survey of meteorite physical properties: Density, porosity and magnetic susceptibility. Ph.D. Thesis. University of Florida, Orlando, Florida, USA.
Maksimova, A.A., Petrova, E.V., Chukin, A.V., Nogueira, B.A., Fausto, R., Szabó, Á., Dankházi, Z., Felner, I., Gritsevich, M., Kohout, T., Kuzmann, E., Homonnay, Z., Oshtrakh, M.I., 2021. Bjurböle L/LL4 ordinary chondrite properties studied by Raman spectroscopy, X-ray diffraction, magnetization measurements and Mössbauer spectroscopy. Spectrochim. Acta A Mol. Biomol. Spectrosc. 248, 119196 https://doi.org/10.1016/j.saa.2020.119196.
Marxen, J.C., Prymak, O., Beckmann, F., Neues, F., Epple, M., 2008. Embryonic shell formation in the snail Biomphalaria glabrata: a comparison between scanning electron microscopy (SEM) and synchrotron radiation micro computer tomography (SRμCT). J. Molluscan Stud. 74 (1), 19–26. https://doi.org/10.1093/mollus/eym044.
Miyamoto, M., 1991. Thermal metamorphism of CI and CM carbonaceous chondrites: an internal heating model. Meteoritics 26, 111–115. https://doi.org/10.1111/j.1945-5100.1991.tb01026.x.
Miyamoto, M., Fujii, N., Takeda, H., 1981. Ordinary chondrite parent body – an internal heating model. Lunar Planet. Sci. Conf. Proc. 12, 1145–1152.
Münch, B., Trtik, P., Marone, F., Stampanoni, M., 2009. Stripe and ring artifact removal with combined wavelet—Fourier filtering. Opt. Express 17 (10), 8567–8591. https://doi.org/10.1364/oe.17.008567.
Opeil, C.P., Consolmagno, G.J., Safarik, D.J., Britt, D.T., 2012. Stony meteorite thermal properties and their relationship with meteorite chemical and physical states. Meteorit. Planet. Sci. 47 (3), 319–329. https://doi.org/10.1111/j.1945-5100.2012.01331.x.
Opeil, C.P., Britt, D.T., Macke, R.J., Consolmagno, G.J., 2020. The surprising thermal properties of CM carbonaceous chondrites. Meteorit. Planet. Sci. 55 (8) https://doi.org/10.1111/maps.13556.
Ostrowski, D.R., Bryson, K.L., 2019. The physical properties of meteorites. Planet. Space Sci. 165, 148–178. https://doi.org/10.1016/j.pss.2018.11.003.
Paganin, D., Mayo, S.C., Gureyev, T.E., Miller, P.R., Wilkins, S.W., 2002. Simultaneous phase and amplitude extraction from a single defocused image of a homogeneous object. J. Microsc. 206, 33–40. https://doi.org/10.1046/j.1365-2818.2002.01010.x.
Peyrin, F., Mastrogiacomo, M., Cancedda, R., Martinetti, R., 2007. SEM and 3D synchrotron radiation micro-tomography in the study of bioceramic scaffolds for tissue-engineering applications. Biotechnol. Bioeng. 97 (3), 638–648. https://doi.org/10.1002/bit.21249.
Pietzsch, T., Preibisch, S., Tomančák, P., Saalfeld, S., 2012. Imglib2–generic image processing in java. Bioinformatics 28, 3009–3011. https://doi.org/10.1093/bioinformatics/bts543.
Preibisch, S., Saalfeld, S., Tomancak, P., 2009. Globally optimal stitching of tiled 3D microscopic image acquisitions. Bioinformatics 25 (11), 1463–1465. https://doi.org/10.1093/bioinformatics/btp184.
Ramos Oliveira, G.J., Horta, D.G., da Silva, F.L., von Krüger, F.L., Silva, G.J.B., Mazzinghy, D.B., 2021. Evaluation of mineral liberation and stereological bias based

on X-ray microtomography and scanning electron microscopy for an iron ore tailing. Miner. Process. Ext. Metall. 1–10 https://doi.org/10.1080/25726641.2021.1965775.
Ramsay, W., Borgström, L.H., 1902. Der Meteorit von Bjurböle bei Borgå von Wilhelm Ramsay u. LH Borgström. K. Malmström in Kuopio.
Rushmer, T.A., Clark, S.M., Parkinson, D., 2013. Chondrules as natural analogs for metal segregation: analyses from 3D synchrotron imaging. In: AGU Fall Meeting Abstracts, Vol. 2013, pp. P51A–1722.
Rutherford, M.E., Chapman, D.J., Derrick, J.G., Patten, J.R., Bland, P.A., Rack, A., Collins, G.S., Eakins, D.E., 2017. Probing the early stages of shock-induced chondritic meteorite formation at the mesoscale. Sci. Rep. 7 (1), 1–10. https://doi.org/10.1038/srep45206.
Sasso, M.R., Macke, R.J., Boesenberg, J.S., Britt, D.T., Rivers, M.L., Ebel, D.S., Friedrich, J.M., 2009. Incompletely compacted equilibrated ordinary chondrites. Meteorit. Planet. Sci. 44 (11), 1743–1753. https://doi.org/10.1111/j.1945-5100.2009.tb01204.x.
Schindelin, J., Arganda-Carreras, I., Frise, E., Kaynig, V., Longair, M., Pietzsch, T., Preibisch, S., Rueden, C., Saalfeld, S., Schmid, B., Tinevez, J.Y., 2012. Fiji: an open-source platform for biological-image analysis. Nat. Methods 9 (7), 676–682. https://doi.org/10.1038/nmeth.2019.
Scott, E.R.D., Krot, T.V., Goldstein, J.I., Wakita, S., 2014. Thermal and impact history of the H chondrite parent asteroid during metamorphism: constraints from metallic Fe-Ni. Geochim. Cosmochim. Acta 136, 13–37. https://doi.org/10.1016/j.gca.2014.03.038.
Soini, A.-J., Kukkonen, I., Kohout, T., Luttinen, A., 2020. Thermal and porosity properties of meteorites: a compilation of published data and new measurements. Meteorit. Planet. Sci. 55, 402–425. https://doi.org/10.1111/maps.13441.
Soini, A.-J., Kukkonen, I.T., Suhonen, H., Lukic, B., Kohout, T., Luttinen, A.V., 2022. SEM imaging data used in "Investigation of the porosity of L/LL4 ordinary chondrite Bjurböle using synchrotron radiation microtomography and scanning electron microscopy: implications for parent body evolution". Zenodo. https://doi.org/10.5281/zenodo.6504815.
Soini, A.-J., Kukkonen, I., Suhonen, H., Lukic, B., Kohout, T., Luttinen, A., 2023. Phase contrast imaging of fall L/LL4 ordinary chondrite Bjurböle (Version 1). European Synchrotron Radiation Facility. 10.15151/ESRF-DC-1163775534.
Song, S.B., Liu, J.F., Yang, D.S., Ni, H.Y., Huang, B.X., Zhang, K., Mao, X.B., 2019. Pore structure characterization and permeability prediction of coal samples based on SEM images. J. Nat. Gas Sci. Eng. 67, 160–171. https://doi.org/10.1016/j.jngse.2019.05.003.
Starborg, T., O'Sullivan, J.D., Carneiro, C.M., Behnsen, J., Else, K.J., Grencis, R.K., Withers, P.J., 2019. Experimental steering of electron microscopy studies using prior X-ray computed tomography. Ultramicroscopy 201, 58–67. https://doi.org/10.1016/j.ultramic.2019.03.002.
Strait, M.M., 2010. The appearance of porosity in meteorites. Meteorit. Planet. Sci. Suppl. 73, 5259.
Supek, F., 2015. Available online at: https://code.google.com/archive/p/fast-random-forest/ (March 23, 2023).
Tankyevych, O., Talbot, H., Dokladal, P., 2008. Curvilinear morpho-Hessian filter. In: 2008 5th IEEE international symposium on biomedical imaging: from nano to macro, proceedings, ISBI, 1011–4. https://doi.org/10.1109/ISBI.2008.4541170.
Taylor, G.J., Maggiore, P., Scott, E.R.D., Rubin, A.E., Keil, K., 1987. Original structures, and fragmentation and reassembly histories of asteroids: evidence from meteorites. Icarus 69, 1–13. https://doi.org/10.1016/0019-1035(87)90002-9.
Terho, M., Pesonen, L.J., Kukkonen, I.T., 1993. Petrophysical classification of meteorites: new results. Open File Report. Q 29, 1/91/1, Geophys. Dep. Geol. Surv. Fini.
Tsuchiyama, A., Uesugi, K., Nakano, T., Ikeda, S., 2005. Quantitative evaluation of attenuation contrast of X-ray computed tomography images using monochromatized beams. Am. Mineral. 90 (1), 132–142.
Wilkison, S.L., McCoy, T.J., McCamant, J.E., Robinson, M.S., Britt, D.T., 2003. Porosity and density of ordinary chondrites: clues to the formation of friable and porous ordinary chondrites. Meteorit. Planet. Sci. 38 (10), 1533–1546. https://doi.org/10.1111/j.1945-5100.2003.tb00256.x.
William, W., Ware, A., Basaza-Ejiri, A.H., Obungoloch, J., 2019. A pap-smear analysis tool (PAT) for detection of cervical cancer from pap-smear images. Biomed. Eng. Online 18 (1), 1–22. https://doi.org/10.1186/s12938-019-0634-5.
Yomogida, K., Matsui, T., 1984. Multiple parent bodies of ordinary chondrites. Earth Planet. Sci. Lett. 68 (1), 34–42. https://doi.org/10.1016/0012-821X(84)90138-9.
Zhang, J., Yu, L., Jing, H., Liu, R., 2018. Estimating the effect of fractal dimension on representative elementary volume of randomly distributed rock fracture networks. Geofluids 2018. https://doi.org/10.1155/2018/7206074.
Zou, G., She, J., Peng, S., Yin, Q., Liu, H., Che, Y., 2020. Two-dimensional SEM image-based analysis of coal porosity and its pore structure. Int. J. Coal Sci. Technol. 7 (2), 350–361. https://doi.org/10.1007/s40789-020-00301-8.